Energy Dissipation during Geomagnetic Storms

Author:

Fatemeh BAGHERI

Supervisor:

Dr. Ramon E. LOPEZ

A thesis submitted in fulfillment of the requirements

for the degree of Doctor of Philosphy of Science

in the

Department of Physics

December 2021

Declaration of Authorship

I, Fatemeh BAGHERI, declare that this thesis titled, "Energy Dissipation during Geomagnetic Storms" and the work presented in it are my own. I confirm that:

- This work was done wholly or mainly while in candidature for a research degree at this University.

- Where any part of this thesis has previously been submitted for a degree or any other qualification at this University or any other institution, this has been clearly stated.

- Where I have consulted the published work of others, this is always clearly attributed.

- Where I have quoted from the work of others, the source is always given. With the exception of such quotations, this thesis is entirely my own work.

- I have acknowledged all main sources of help.

- Where the thesis is based on work done by myself jointly with others, I have made clear exactly what was done by others and what I have contributed myself.

Signed:

_____

Date:

_____

UNIVERSITY OF TEXAS ARLINGTON

Abstract

Faculty Name

Department of Physics

Doctor of Philosphy of Science

Energy Dissipation during Geomagnetic Storms

by Fatemeh BAGHERI

vi

Some fraction of the solar wind energy is transferred to the Earth magneto-sphere and ionosphere. Sometimes this transfer of energy is exceptionally large, producing a magnetic storm. Storms occur when the Interplanetary Magnetic Field (IMF) turns southward and remains southward for an extended period of time. During the main phase of many magnetic storms, the solar wind Mach number is low, and IMF magnitude is large. Under these conditions, the iono-spheric potential saturates, and it becomes relatively insensitive to further in-creases in the IMF magnitude. On the other hand, the dayside merging rate and the potential become sensitive to the solar wind density. This should result in a correlation between the intensity of the auroral electrojets and the solar wind density. In this study, I find several storm events to examine the effect of the solar wind density on the intensity of the auroral electrojets (as measured by the SME index) under the condition of low Mach number and steady IMF. As ex-pected, there is a positive correlation between solar wind density and the SME index. I show that this correlation coefficient gets larger for smaller Mach num-ber when one would expect the effect of density to be more significant.

Furthermore, I study the role of solar wind density during an event with the small northward IMF. In the case of northward IMF, since the reconnection re-gions are limited, the changes of the ionospheric potential caused by the viscous interaction can be greater/comparable to the reconnection-driven potential. I show that the solar wind density and the SME index correlate with small north-ward IMF during the event. Thus, the solar wind density correlations with the

auroral electrojets have the same behavior under two conditions: 1) in the saturation regime and 2) in the event with northward IMF, although very different physics drove them.

Moreover, I provide a sample of 314 moderate to strong storms and investigate the correlation between the Dst index and the energy dissipated in the ionosphere. I show that, on average, for the lower Mach number, this correlation decreases. I also show that the ionospheric indices of the storms with the lower Mach number are less correlated to the geoeffectiveness of the solar wind during these storms.

As a next step to studying the energy dissipation during the magnetic storms, I study the energy dissipated in the ionosphere through frictional heating, generally referred to as Joule heating. There are several empirical models to estimate Joule heating based on ionospheric currents using the AE index. In this study, I select 12 magnetic storms from the CCMC database and compare the integrated joule heating with the results of empirical models. I also use the SWMF global magnetohydrodynamic simulations for 13 storms to reproduce the correlation between the simulated AE index and simulated Joule heating to examine the empirical models. I find that the scale factor in the empirical model is half the predicted using the SWMF simulations.

Finally, at the end of the dissertation, I point out the possible future studies.

Acknowledgements

I thank my advisors Dr. Ramon Lopez. Having spent more than a decade within academia and higher education, I cannot not imagine any academic advisers who could be more supportive and caring about their students as he has been to me.

In addition, I acknowledge Dr. Qiming Zhang for his incredible kindness and help.

Last but not least, I thank my husband, Dr. Amir Shahmoradi, for believing in me and for his endless support and love.

Contents

List of Figures

List of Tables

Chapter 1

Introduction

1.1 Drivers of Space Weather

Space Weather refers to conditions on the Sun and in the solar wind, magnetosphere, ionosphere, and thermosphere that can influence the performance and reliability of space-borne and ground-based technological systems and endanger human life and health. Adverse conditions in the space environment can cause disruption of satellite operations, communications, navigation, and electric power grids, leading to a panoply of socio-economic losses.

National Space Weather Program

Strategic Plan (March 1995)

Space weather is the concept of dynamic, highly variable conditions in the geospace environment. The geospace environment includes the solar atmosphere, the interplanetary medium, and the magnetosphere-ionosphere- thermosphere system. The core physics underlying space weather is solar wind-magnetosphere coupling: as the properties of the solar wind change, activity in

the magnetosphere changes. Therefore, research of space weather is the study of the large-scale energy and matter eruptions from the solar activity region, the propagation and evolution of the solar winds, and the significant changes in the geomagnetic activity in the Earth's magnetosphere-ionosphere system as a response to the energy carried through interplanetary space by the solar wind. The other main focus of research in space weather is studying the effects of changes in the geospace environment on human activities such as the safety of astronauts, electromagnetic-based communications, GPS systems, and the operation of electric power grids.

In the 20th century, the interest in space weather expanded as military and commercial systems depended on systems affected by space weather. The modern scientific basis of physics of solar-wind/magnetosphere coupling originates from two ideas published in 1961 (Axford & Hines, 1961; Dungey, 1961). The development of technology in this century provides the quantitative data-analysis study of solar-wind/magnetosphere coupling started in earnest with the works of Heppner et al. (1963) and Snyder et al. (1963), published shortly after the first spacecraft measurements of the solar wind were made. Using data analysis and computer simulations, 60 years of work after 1961 by the international space-physics community has delivered a lot of progress on this topic (Borovsky, 2021).

Three phenomena originating from the Sun are the three main solar drivers of space weather: Solar flares, Coronal Mass Ejections (CMEs), and High Speed Streams. In the following, I briefly describe them.

- **Solar flares** are massive explosions on the Sun. A flare appears as a sudden, intense brightening region on the Sun, typically lasting several minutes to hours. Flares are seen as bright areas on the Sun in x-rays, optical wavelengths, and noise bursts in radio wavelengths. The primary energy of flares is the release of energy stored in strong magnetic fields. The electromagnetic emission produced during flares travels at the speed of light, taking about 8 minutes to reach Earth—rapidly affecting the dayside of Earth.

- **CMEs** Coronal Mass Ejections are explosive outbursts of plasma from the Sun's outer atmosphere, the corona. The blast of a CME typically carries roughly a billion tons of material outward from the Sun at speeds as fast as thousands of kilometers per second. A CME contains hot plasma and powerful magnetic fields. They can have a long period of southward IMF, which causes severe disturbance in the magnetosphere system, called geomagnetic storms. In contrast to solar flares, CMEs may take hours to erupt from the Sun entirely and typically take 1-4 days to travel to Earth.

- **High Speed Streams and Corotating Interaction Region** High speed streams (HSS), with speeds exceeding 700 km/s, are originated in the coronal holes, as confirmed by Ulysses observations (Phillips et al., 1994). Coronal holes, which appear as dark areas in x-ray solar images (Krieger et al., 1973; Timothy et al., 1975), are regions in the Sun that are less dense than the surrounding plasma. In these regions, the magnetic field lines are open. Therefore the solar wind escapes more readily into space, resulting in streams of relatively fast solar wind. As the high speed stream interacts with the

relatively slower solar wind, the plasma at the boundary gets compressed so that the density and IMF in the slow solar wind region increases. These compression regions are known as corotating interaction regions (CIR). The pattern of interaction regions is repeated each time the Sun rotates, and they are called corotating interaction regions (CIRs) (Smith & Wolfe, 1976). Although the primary driver of the geomagnetic storms is CMEs, strong CIRs and the HSS also produce southward IMF. Therefore, they can impact Earth's magnetosphere-ionosphere system. However, since they do not have a long period of southward IMF, it is rare to cause intense geomagnetic storms.

In addition, solar particles events are the release of large numbers of high-energy charged particles, which are accelerated to large fractions of the speed of light. Electrons are accelerated in flares, and shock waves accelerate protons. These high-energy particles can also affect space weather.
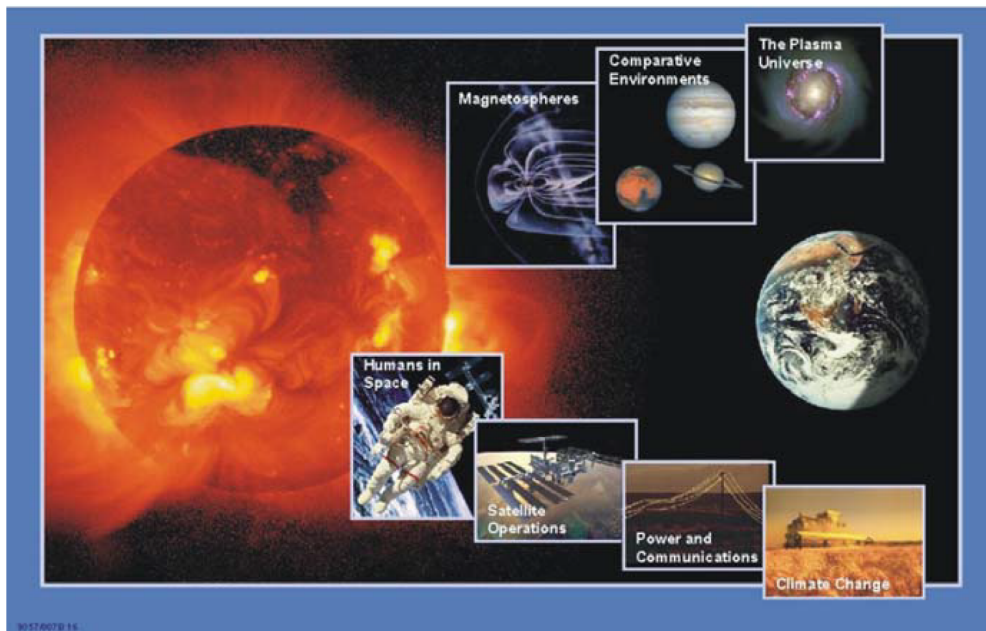
FIGURE 1.1: Scientific and applications-related aspects of the Sun-Earth Connections research (credit: NASA)

1.2 Magnetosphere

The magnetosphere is the outermost region of the geospace. The interaction of the solar wind with the magnetosphere is the key element of the space weather cause-and-effect chain process from the Sun to Earth, which is one of the most challenging scientific problems in geospace weather study. The magnetosphere is formed when the solar wind interacts with the Earth's internal magnetic field.

When the supersonic solar wind passes the *bow shock*, the boundary at which the speed of the solar wind decreases as a result of its approach to the magnetosphere, it (solar wind) gets compressed, and its speed significantly decreases

and deflects around the magnetosphere. The boundary of the magnetosphere and the surrounding plasma is called *magnetopause*. The location of the magnetopause is determined by the balance between the pressure of the dynamic planetary magnetic field and the dynamic pressure of the solar wind. As the solar wind pressure increases and decreases, the magnetopause moves inward and outward in response. It has a bullet shape, about 15 Re (Earth radii) abreast of the Earth and on the night side (in the *magnetotail*) approaching a cylinder with a radius of 20–25 Re. The tail region stretches well past 200 Re, and the way it ends is not well known. The structure and motion of the plasma and its associated magnetic field result in currents in the magnetosphere and ionosphere.

1.2.1   Magnetospheric Currents

To describe magnetospheric currents and dynamics, as Vasyliūnas (2001) discussed, it is important to know which quantity is the cause of which? There are two sets of quantities that might be considered as a fundamental or primary quantities based on the Maxwell's equations: 1) magnetic field (**B**) and velocity (**v**), or 2) electric field (**E**) and current density (**J**). However, Vasyliunas, 2005 showed that the {**B, v**} set is the primary quantities if the system has dynamic ($\partial/\partial t \neq 0$). But, in a stationary case, we can describe the system by considering the **E** and **J** as the primary quantities.

The magnetospheric currents can be classified as 1) boundary currents, (2) ring current, (3) ionospheric currents, (4) field-aligned currents, (5) magnetotail currents, and (6) bow shock current. The existence of these currents can be explained in the paradigm of **{B, v}** as follows:

- **Boundary Currents**: The magnetopause separates the weaker magnetic field in the magnetosheath from the stronger field within the magnetosphere, which means at that region, the divergence of the magnetic field is not zero ($\nabla \times \vec{B} \neq 0$). Hence there is a current at the Earth's magnetosphere boundary, called the *Chapman–Ferraro* current. These currents flow, dawn-to-dusk across the nose of the magnetosphere and dusk-to-dawn across the magnetotail magnetopause (Chapman & Ferraro, 1931).

- **Ring Current**: In the equatorial plane of the magnetotail, where the pressure of hot plasma causes an inhomogeneous magnetic field, there is a current due to the motion of trapped particles (Chapman & Ferraro, 1941; Chapman & Ferraro, 1931). The ring current lies in the equatorial plane at a distance of 3 to 8 R_E. It consists of ions, most of which are protons, that circulate clockwise around the Earth (when viewed from the north). The particles of this region produce a magnetic field in opposition to the Earth's magnetic field. During a geomagnetic storm (which will be discussed later), the number of particles in the ring current will increase. As a result, there is a decrease in the effects of the geomagnetic field. Generally, ring current is not included in the Magneto-Hydro-Dynamics (MHD) simulation because the underlying physics of MHD is cold plasma.

- **Ionospheric Currents**: The density of particles in ionospheres is high enough that collisions cannot be ignored. Collisions give rise to momentum transfer, and electrical conductivity is important. The generalized Ohm's law can describe current flows in ionospheres. The ionospheric current is made up of two components: Pedersen and Hall currents which flow perpendicular to each other; Pederson currents are parallel to, and Hall currents are perpendicular to the electric field. Hall currents generally flow along closed paths within the ionosphere and are responsible for significant magnetic perturbations on the ground that are observable from within the auroral oval and the polar caps.

- **Field-aligned Currents**: Field-aligned currents flow along the magnetic field lines, and they connect the Earth's magnetosphere to the Earth's high latitude ionosphere. These currents were predicted in 1908 by Norwegian physicist Kristian Birkeland, so the also called *Birkeland currents* (Birkeland, 1903). The Birkeland currents occur in two regions. The Birkeland currents-*region 1* extends from noon through the dusk to the midnight sector on the high latitude sheet of the auroral zone, while The Birkeland currents-*region 2* extends from noon through the dawn to the midnight sector on the low latitude sheet (Iijima & Potemra, 1976).

- **Magnetotail Currents**: Magnetotail currents are responsible for the long magnetic tails of planetary magnetospheres. Understanding the origin of magnetotail currents is important because they are tied to mechanisms that

transfer the solar wind mass, momentum, and energy into planetary magnetic fields. The magnetotail currents are also a significant source for auroral currents since tail currents are diverted into the ionosphere along the magnetic field during an aurora. The *current sheet* (or *neutral sheet*) is at the center of the magnetotail, which separates the north and south lobes. The current in the current sheet is called the **cross-tail current** (figure 1.3), and it flows from dawn to dusk.

- **Bow Shock Current**: As mentioned earlier, as the solar wind passes the bow shock, it gets compressed. Therefore, the curl of the magnetic field around the bow shock is not zero. This implies that there is a current at bow shock which needs to be closed somewhere and delivers the electromagnetic energy generated at the shock to a load in the system. Some of the bow shock current closes through the Chapman-Ferraro currents at the magnetopause, and some closes directly through the ionosphere on open field lines. In figure 1.2, the bow shock current is schematically illustrated.
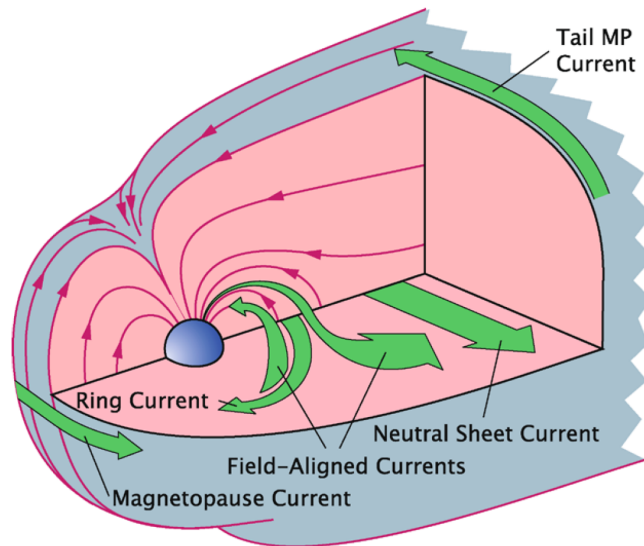
FIGURE 1.2: A Schematic view of magnetospheric current systems.
Bow shock current is not included.
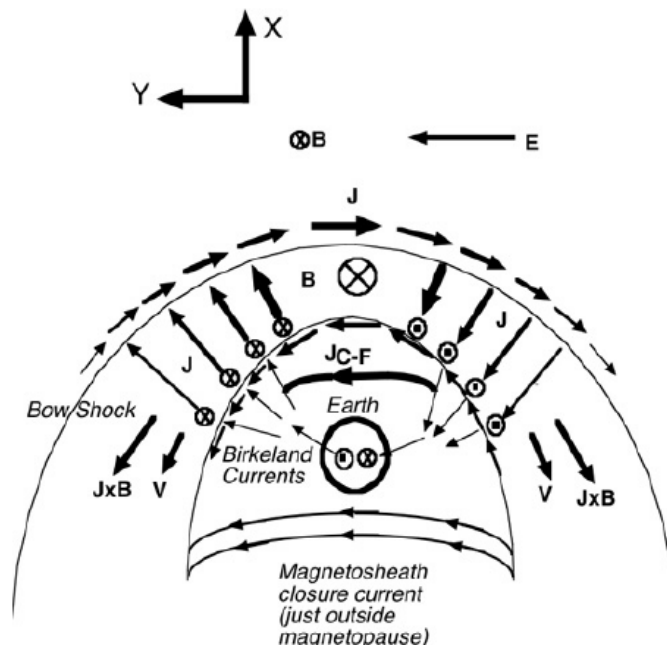
FIGURE 1.3: A Schematic view of bow shock current (Lopez, 2018).

1.3 Coupling of Solar Wind to Geospace

Two methods were proposed to explain how plasma can be transported and energized within the magnetosphere in the same year, 1961:

- **Magnetic reconnection** between the IMF and Earth's field,

- **Viscous-like coupling** to the flow outside the magnetosheath (Axford & Hines, 1961; Dungey, 1961).

In the following, I will briefly explain the concept of these ideas.

1.3.1 Magnetic Reconnection

Magnetic reconnection, which is breaking and reconnecting of oppositely directed magnetic field lines in plasma, was motivated by the study of solar fares (Giovanelli, 1947, 1948; Giovanelli, 1939) in the solar atmosphere (the corona); It was quickly realized (Dungey, 1953; Hoyle, 2014) that the same magnetic reconnection process in solar flares also occurs in Earth's magnetic field (Hesse & Cassak, 2020). Figure 1.4 schematically illustrates the magnetic reconnection between two oppositely directed field lines.

In 1961, Dungey proposed that magnetic reconnection is the major driver of magnetosphere dynamics (Dungey, 1961). Magnetic reconnection occurs at the magnetopause between the interplanetary magnetic field (IMF) and the Earth magnetic field, and it is the most efficient when the IMF is directed *southward*. IMF orientation is discussed in terms of the usual Geocentric Solar Magnetic

(GSM) coordinate system, in which the X-axis points towards the Sun, the X-Z plane contains the Earth's magnetic axis, and Y is perpendicular to this, pointing in a generally backward direction. In this system, *northwards* and *southwards* directed field relate to IMF $B_Z > 0$ and $B_Z < 0$, respectively.
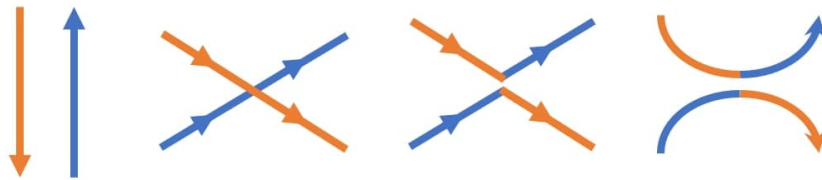
FIGURE 1.4: Schematic diagram of magnetic reconnection: two opposite field lines break and reconnect at the X-point. In this process, magnetic field energy is converted to plasma kinetic and thermal energy.

Reconnection at the magnetopause, which is called the *dayside reconnection*, accelerates and directs anti-sunward a mixture of magnetosheath and magnetospheric plasma along newly opened magnetic field lines to form an extended magnetotail (Cowley et al., 1991; Dungey, 1965; Milan et al., 2004). Then, another reconnection in the central plane of the tail recloses open field lines, which pushes the plasma sunward, allowing a new cycle to begin. This reconnection is called *nightside reconnection*. This 3-stage mechanism is called the **Dungey cycle**. Figure 1.8 shows the stages involved in the Dungey cycle. This concept naturally explains several known features of the magnetosphere, such as the presence of an extended magnetotail, erosion of the dayside magnetopause during periods of southward interplanetary magnetic field (IMF), and the twin-cell ionospheric

convection pattern (Daglis et al., 1999).

Dungey's proposal explained that the cycle is steady-state and that the reconnection rate at dayside and nightside is the same. But, further studies show that the rate of reconnection is variable. The *Dungey cycle timescale* refers to the length of time from the opening of the field lines at the dayside to the closing of the field lines on the nightside, which is approximately 1-hour (Cowley, 1982).
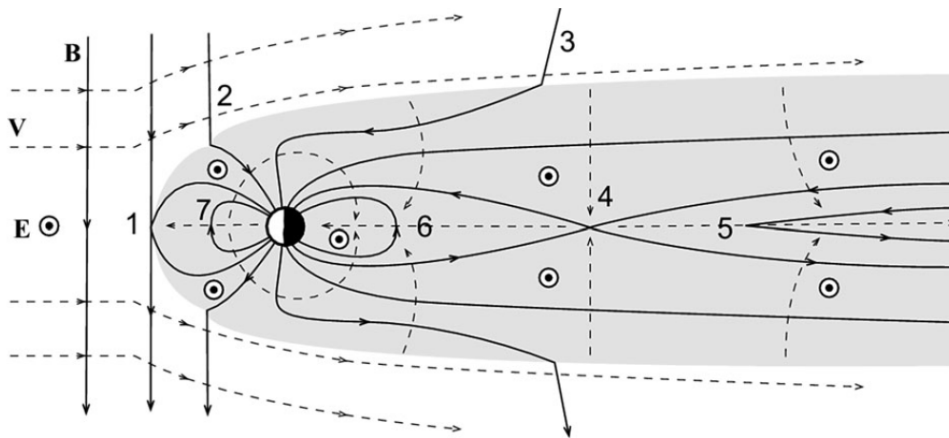
FIGURE 1.5: Schematic diagram showing the stages of the Dungey cycle: 1. in the first stage, dayside reconnection creates an opening in the magnetopause in which the solar wind can enter the magnetosphere. 2. In the second stage, the flux travels in the direction of the solar wind across the magnetosphere. 3. In the third stage, nightside reconnection at the magnetotail closes the open flux, allowing a new cycle to begin (courtesy S. Milan).

In the case of northward IMF, all the reconnection regions are on the dayside. Crooker (1992) suggested a plasma circulation that is opposite to the Dungey cycle and called a *reverse Dungey cycle*. Figure 1.6-*panel-(a)* shows a schematic of a four-cell convection pattern for purely northward IMF. The high-latitude reverse plasma circulation is characterized by a sunward flow at higher latitude

followed by anti-sunward flow at lower latitude (Bhattarai & Lopez, 2013). The outer convection cells are due to the viscous-like interaction, which will be explained in the next section. During northward IMF, magnetic reconnection occurs poleward of the cusp region. Therefore the reconnection closes the field lines on the dayside. As seen in figure 1.7 there is a dense plasma at the nose where the field lines are closed (Bhattarai et al., 2012). The reconnection process under the condition of northward IMF does not put any energy/flux into the tail, and hence, it does not produce geomagnetic storms.
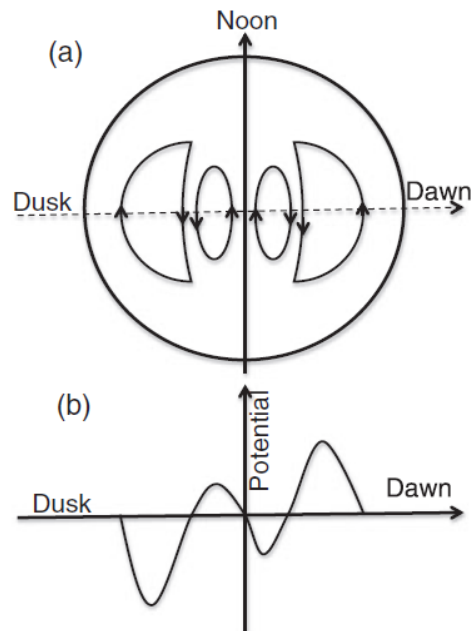
FIGURE 1.6: *(a)* Schematic diagram of a four-cell convection pattern during a purely northward IMF. The inner cells are due to reverse convection, and the outer cells are due to viscous interaction (as discussed later). *(b)* The variation in the potential seen by a satellite moving along the dotted line in *panel-(a)*. Figure is from Bhattarai and Lopez (2013, Figure 2)

.
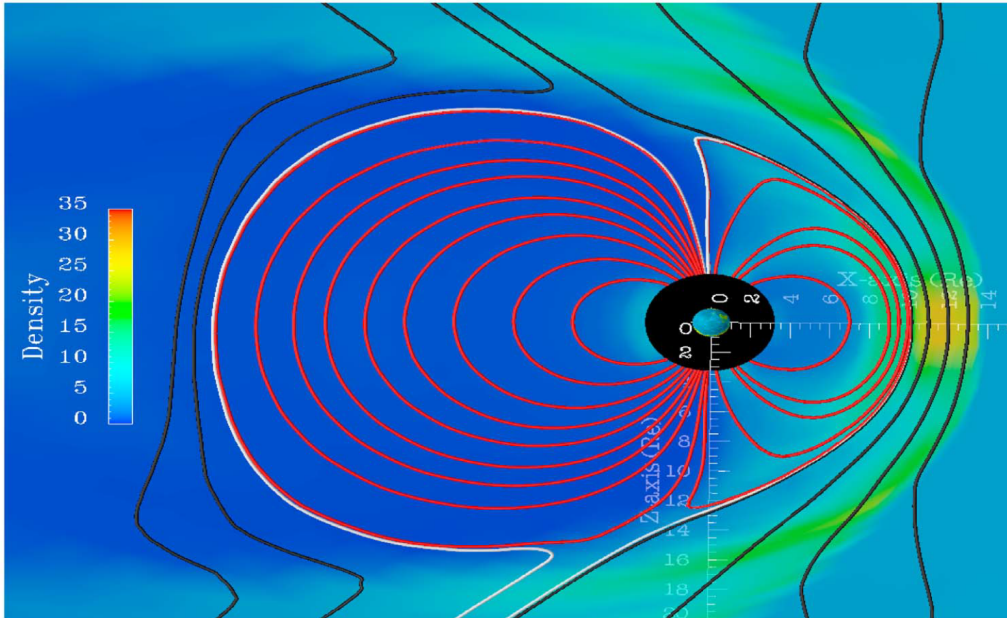
FIGURE 1.7: Visualization of the Lyon-Fedder-Mobarry (LFM) simulation results in the X-Z plane showing the high-latitude reconnection topology during purely northward IMF (10 nT). The Sun is on the right side of the picture. Solar wind field lines, reconnected field lines, and closed field lines are drawn in black, white, and red color, respectively, and the plasma density is color-coded. Figure and caption from Bhattarai et al. (2012, Figure 2)

.

The dayside reconnection region is used to define the ***geoeffective length***. The geoeffective length is the length in the solar wind perpendicular to the IMF and to the solar wind flow that intersects the dayside merging region. The magnetic flux across this length is the flux that is merged with the geomagnetic field, producing convection in the ionosphere-magnetosphere system. The changes in the ionospheric potential via the reconnection process is proportional to the geoeffective length,

$$\frac{d\phi}{dt} = LVB_s \tag{1.1}$$

where L is the geoeffective length, V is the solar wind speed, and B_s is the southward component of the IMF.
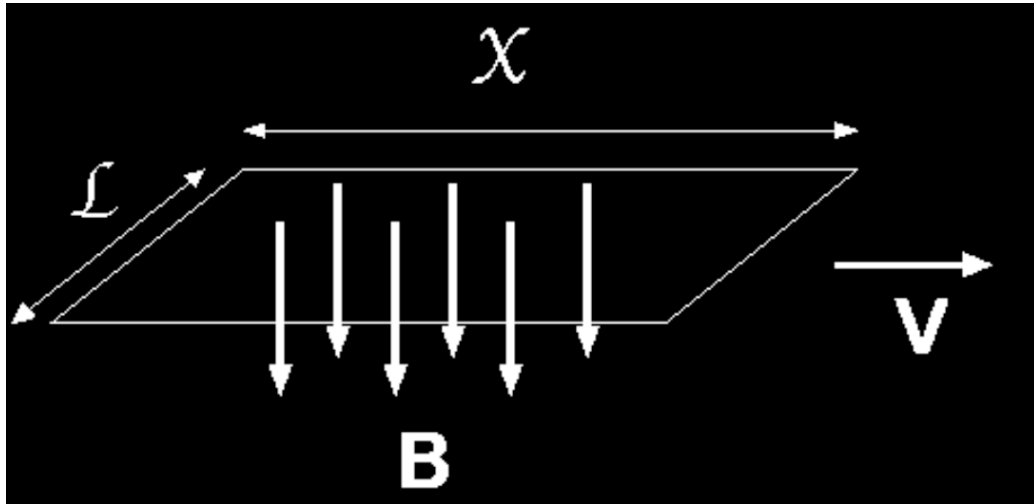
FIGURE 1.8: Schematic diagram of the geoeffective length shown as L and how that controls the gereneration of the reconnection potential (courtesy R. Lopez).

1.3.2 Viscous-like Interaction

The ionospheric potential is mostly driven by magnetic reconnection. However, magnetic reconnection is not the only process that contributes to the ionospheric potential. It was shown that the ionospheric convection flow rate is approximately proportional to B_s, where $B_s = |B_z|$ for $B_z \leq 0$ nT (Cowley, 1984; Reiff et al., 1981; Weimer, 2001), which has the value of $50 - 100$ kV, on average. But, when the IMF $B_z \geq 0$ nT ($B_s = 0$ nT), the sub-solar reconnection is expected to cease, and therefore it was thought that the ionospheric potential should be zero. However, as noted by Reiff et al. (1981) and Weimer (2001), the cross-polar cap potential remains non-zero, taking an average value of a few 10 s of kV under

such situations. MHD simulations are also showed that residual potential when the merging rate goes zero (Lopez et al., 2010). Using the Lyon-Fedder-Mobarry (LFM) MHD simulations, Bruntz et al. (2012) found that the linear fit of the ionospheric potential with IMF-B_z has a non-zero intercept. Moreover, based on an LFM simulation with zero-IMF, they found there is still a non-zero ionospheric potential with the amount that is consistent with the linear fit. As outlined by Axford and Hines (1961), the non-zero ionospheric potential under the condition of small IMF can be explained by a **Viscous-Like** interaction between the solar wind and the plasma inside the magnetosphere.

The viscous-like interaction can be understood by looking at the Low Latitude Boundary Layer (LLBL). In this region, the anti-sunward flow in the magnetosheath is viscously coupled with the flow inside the magnetosphere. Hence, the flow inside the magnetosphere is dragged toward the tail. This flow continues to circulate from tail to noon and make a *viscous cell*. This pattern of the flow is projected to the ionosphere via Birkeland region-I currents at low latitudes. It is illustrated schematically in 1.9. An important mechanism to enable this interaction is the Kelvin-Helmholtz instability driven by flow shear at the magnetopause; Therefore, the viscous-like interaction is significantly enhanced by the growth of the Kelvin-Helmholtz instability at LLBL (Axford, 1964).
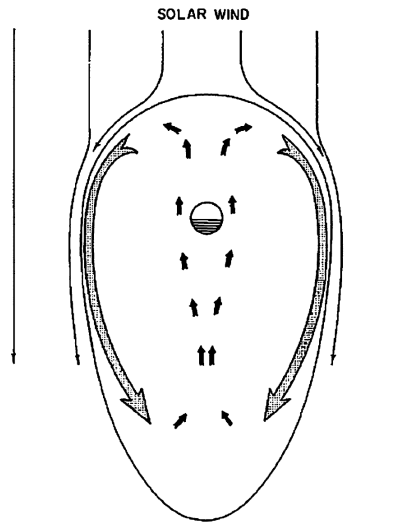
FIGURE 1.9: Schematic diagram showing the circulation of plasma through the magnetosphere, as proposed by Axford and Hines (1961), driven by a "viscous-like" interaction with the solar wind (Seki et al., 2015).

Both processes, magnetic reconnection, and viscous-like interaction, extend the magnetic field in the tailward direction, forming a magnetotail (Vasyliūnas, 2011). The viscous-like interaction also involves magnetic reconnection on a small scale (Hasegawa et al., 2004; Nykyri et al., 2006). Bruntz et al. (2012) used the Lyon-Fedder-Mobarry (LFM) magnetohydrodynamic simulation to investigate the response of the viscous potential to a variety of ideal conditions both in the solar wind and the ionosphere. Their results show that the viscous potential in LFM increases with either increasing solar wind density or velocity, with a relationship that is consistent with the previous empirical model of Newell et al. (2008).

1.3.3 Saturation of Ionospheric Potential: Force Balance Model

The physical process behind energy transfer to the magnetosphere-ionosphere system during a geomagnetic storm can be significantly different when the solar wind has a low Mach number (< 3.5). The difference arises since under the condition of low Mach number, the transpolar potential saturates (Lopez et al., 2010) so that the potential becomes independent of the IMF magnitude. The saturation effect can be understood by considering the steady-state momentum equation,

$$\rho \frac{d\vec{V}}{dt} = \rho \vec{V}.\nabla \vec{V} = -\nabla P + \vec{J} \times \vec{B} . \tag{1.2}$$

The balance between the two forces, $\vec{J} \times \vec{B}$ and $-\nabla P$, explains the divergence of the magnetosheath flow, which regulates the geoeffective length in the solar wind and the rate of energy transfer to the system. The main point is that when the IMF is large, and the Mach number is low, the $\vec{J} \times \vec{B}$ term dominates the right-hand side of the momentum equation. Increasing the IMF under these conditions increases the $\vec{J} \times \vec{B}$ and the divergence of the flow, reducing the geoeffective length in the solar wind. Consequently, less flow can reach the merging line, leading to the saturation of the ionosphere potential (Lopez et al., 2010). In this **saturation** regime, the energy transfer is controlled by the density of the solar wind, since the divergence of the flow, and thus the geoeffective length, would be inversely proportional to the flow density (Lopez et al., 2004; Shue & Kamide, 2001).

However, the ring current injection rate does not saturate when the ionospheric potential saturates (Russell et al., 2001). For higher values of solar wind IMF, the reconnection region moves closer to Earth. Closed flux tubes created by the closer reconnection regions have smaller volume per uint magnetic flux and can penetrate deeper into the inner magnetosphere(Lopez et al., 2009). Thus, the injection of particles into the inner magnetosphere produces more energization, and the ring current energy content, hence Dst, continues to depend on the magnitude of the IMF. Therefore, one can conclude that under the condition of low Mach number solar wind, the ring current (and so, the Dst Index) continues to respond to the changes of the magnitude of the southward component of the IMF. However, the potential of the polar cap and consequently the auroral electrojet intensity do not continue to respond strongly to IMF variations when the $\vec{J} \times \vec{B}$ term becomes dominant in regulating the reconnection potential. Therefore, using the Dst index can be a misleading indicator of the strength of the geomagnetic storms under these conditions.

1.4 Geomagnetic Storms and Ring Current Indices

Variation in the solar wind generates significant changes in the fields and plasmas in Earth's magnetosphere. As a result, there is a substantial exchange of energy from the solar wind into the magnetosphere. This exceptionally large disturbance of the magnetosphere magnetic field, which remains for an extended period of time called a **geomagnetic storm**.

George Graham was the first one who observed the first persistent disturbance of the magnetic field in 1722 (Graham, 1724). Later on, Alexander von Humboldt, based on his observation of the magnetic storm that happened on December 21, 1806, found that the presence of aurora is related to the magnetic disturbance. He found that when the aurora disappeared at dawn, there were no magnetic perturbations as well. He called this phenomenon the magnetic storm (Magnetische Ungewitter) (Lakhina & Tsurutani, 2016).

As Gonzalez et al. (1994) discussed, the main feature in the solar wind that is responsible for creating geomagnetic storms is an extended period of southward directed Interplanetary Magnetic field (IMF). Singer (1956) proposed that particles from the solar wind can be trapped in specific regions. He suggested that the gradient drift of the energetic particles trapped in the geomagnetic field carries a westward electric current, called **ring current** (Singer, 1957). The trapped energetic ions consisting ring current has energies 10-200 keV (Frank, 1967; Smith and Hoffman, 1973; Williams, 1981), which effectively decreases the horizontal component of the magnetic field in the vicinity of the Earth.

During a geomagnetic storm, a strong southward interplanetary magnetic field (IMF) reconnects with the Earth's magnetic field and allows solar wind energy transfer into the magnetosphere. Hence the ring current is strongly enhanced, which causes a severe decrease in the strength of Earth's horizontal magnetic field at the surface. Several processes have been proposed to explain the global ring current enhancement empirically and theoretically (Daglis et al.,

1999):

- the inward transport of plasma sheet particles by an enhanced convection electric field,

- the particle injection associated with a substorm,

- the diffusive transport of energetic particles due to the magnetic and/or the electric fluctuations,

- the inward displacement of preexisting trapped particles due to an enhanced electric field,

- the direct entry of ions from the polar region into the ring current .
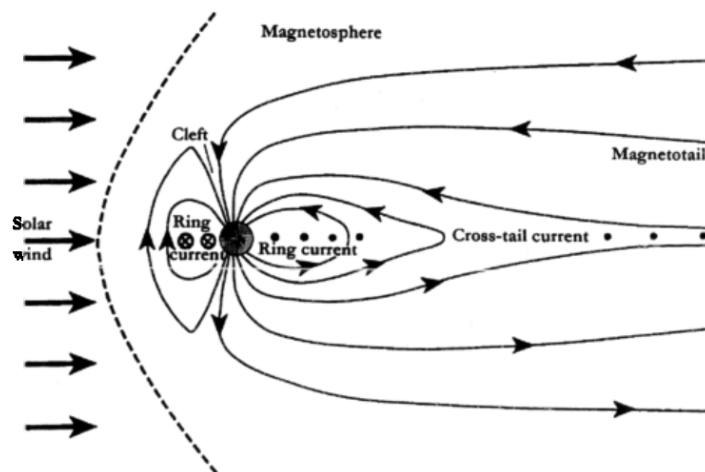
FIGURE 1.10: Schematic outline of the ring current (Daglis et al., 1999).

The total energy in the ring current is related to the disturbance of the magnetic field at the equatorial surface by using *Dessler-Praker-Sckopke* relation. Dessler and Parker (Dessler & Parker, 1959) calculated the perturbation magnetic field

produced at the center of the Earth by azimuthally symmetric ring currents made up of equatorially mirroring, field-aligned, or isotropic monoenergetic particles drifting in a dipole field. They found that the perturbation field is proportional to the total kinetic energy of the ring current particles. Sckopke (1966) demonstrated that Dessler and Parker's result holds for an arbitrary pitch angle distribution, and Carovillano and Maguire (Carovillano & Maguire, 1968) showed that the result holds for an asymmetric ring current in the limit that the self-energy of the ring current magnetic field can be neglected (Greenspan & Hamilton, 2000). The Dessler-Parker-Sckopke relation is

$$\frac{\Delta B}{B_\circ} = \frac{2K}{3U_M} \tag{1.3}$$

where ΔB is the magnetic perturbation at the Earth's center due to the ring current, $B_\circ$ is the equatorial surface field of the particles (ions and electrons), U_M is the energy contained in the Earth's dipole magnetic field outside the surface of the Earth, and K is the kinetic energy of the ring current..

But how can we measure the perturbation field? One can monitor the global strength of the perturbation field using ground-based magnetometers at middle and low latitudes. For instance, we can use the **Dst index** (**D**isturbance **S**torm **T**ime) to estimate of the strength of the disturbance in the surface magnetic field. The Dst index represents the longitudinally averaged part of the external field measured at the geomagnetic dipole equator at the surface of the Earth (Sugiura, 1964). It is provided by the World Data Center for Geomagnetism, Kyoto. Dst is 1-hour data and computed from measurements of the horizontal component of

the magnetic field at four low-latitude ground stations widely spaced in longitude.

Using the Dst index instead of ΔB, we can estimate the kinetic energy of particles in the ring current. However, the Dst index includes not only the disturbance field produced by the ring current but also the disturbance fields due to the magnetopause, tail, and induced currents in the diamagnetic Earth (Campbell, 1996, Sandhu et al., 2021):

- **The magnetopause current:** Enhancements in the magnetopause current contribute positively to the measured magnetic field perturbation, as demonstrated by strong correlations between the solar wind dynamic pressure and the Dst index (Stepanova et al., 2019).

- **The tail current:** The tail current is also a significant contributor to the Dst index, with one estimate being that it is about 25% of the measured perturbation (Turner et al., 2000). Dubyagin et al. (2014) observed a nearly linear relationship between the ring current index and the tail current contribution. They concluded that the tail current is a dominant factor compared to the other additional current systems. Furthermore, Kalegaev et al. (2005) establish that during moderate storm times, the tail current and ring current contributions to ring current indices are comparable, although the tail current contribution is less critical for intense storms. Lopez et al. (2015) found that in one intense storm, the first part of the main phase in Dst/SymH was due entirely to tail currents.

Therefore, Dst^* is defined to correct the Dst index for magnetopause current contributions and induced currents in the solid Earth. Although there are many different ways to correct the index Dst, they generally follow the formulation of Burton et al. (1975):

$$Dst^* = Dst - b\sqrt{P} + c\,nT \tag{1.4}$$

where the parameters b and c are empirically determined and P is the solar wind pressure. In this study, we use the values of b and c determined by O'Brien and McPherron (2000) $b = 7.26nT$ and $c = 11nT$. Therefore by rewriting the Dessler-Parker-Sckopke equation, we have

$$\frac{Dst^*}{B_\circ} = \frac{2K}{3U_M} \; . \tag{1.5}$$

Although the most common index to measure the perturbation field or the ring current energy is the Dst index, but there are a range of *ring current indices* available such as SymH (**Sym**metric **H**orizontal component of a low or midlatitude magnetometer station) index, and the SMR index. All are derived using a similar method, but the main difference is due to the subtraction of baselines, the number of stations used in the calculation, and the cadences of the indices. The SymH index is calculated every minute from a range of ground magnetometers spanning magnetic latitudes from $-47°$ to $50°$. The data are processed in units of one month, and for each month, only six stations that are approximately evenly spaced in longitude are used. For each minute, the disturbance component over the six stations is averaged to provide the SymH index (Iyemori, 1990). As mentioned in the case of Dst, attempts to remove contributions from other current

systems such as magnetopause current to the observed SymH index have been made, resulting in the corrected SymH index. Similar to the Dst^* we can define $Symh^*$ as

$$SymH^* = SymH - 7.26\sqrt{P} + 11 \; nT \; . \tag{1.6}$$

The calculation of the SymH index relies on using observations from magnetometer stations mapping to different MLT sectors of the ring current population and taking an average of those measurements. Therefore, this average perturbation can be considered as describing the symmetric component of the ring current. Alternatively, the AsyH index can be used to describe the asymmetric component of the ring current (Iyemori et al., 1992). The AsyH index is derived similarly to the SymH index. However, the difference between the smallest perturbation and the largest perturbation over the six stations is taken for each minute sample instead of averaging the perturbations.

Newell and Gjerloev (2012) used SuperMAG data collected from several hundred magnetometer stations to introduce the **SMR index**. The method to calculate the 1- minute data of SMR index is conceptually similar to the Dst and SymH index but uses 98 low and midlatitude magnetometers rather than 6 (as is the case for SymH) or 4 (as is the case for Dst).

1.4.1   K and A-Indices

The quasi-logarithmic **K-index** was introduced by Julius Bartels in 1939 (Bartels et al., 1939). The semi-logarithmic K comes from the German word *Kennziffer*
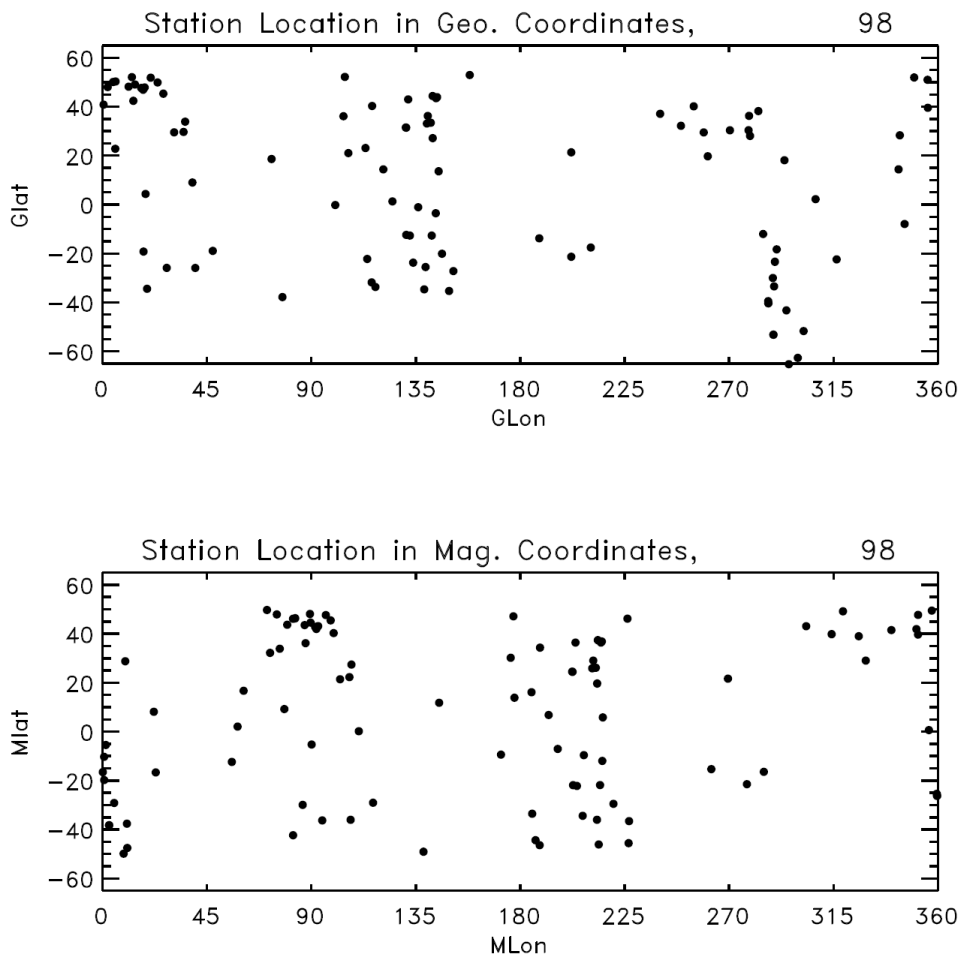
FIGURE 1.11: The distribution of the 98 geomagnetic stations contributing to the SuperMAG regional ring current: (top) geographic coordinates and (bottom) geomagnetic coordinates (Newell & Gjerloev, 2012).

meaning "characteristic digit". This index quantifies disturbances in the horizontal component of Earth's magnetic field with an integer in the range 0–9, with one being calm and five or more indicating a geomagnetic storm. It is derived from the maximum fluctuations of horizontal components observed on a magnetometer during a *three-hour* interval. The **Kp index** is the average K index from 13 stations, and it is the Planetary K-index.

The **A-index** provides a *daily* average level for geomagnetic activity. Because of the non-linear relationship of the K-scale to magnetometer fluctuations, it is not meaningful to take the average of a set of K-indices. What is done instead is to convert each K back into a linear scale called the "equivalent three hourly range" **a-index**. The daily A-index is merely the average of eight a-indices.

1.4.2   Geomagnetic Storm Characterizations

As mentioned earlier, the ring current is the key element of magnetic storms; thus, the most often used definition of a geomagnetic storm is an event wherein the minimum of the Dst index goes below a critical value, for example, -50 nT or -100 nT (Sugiura & Chapman, 1960). In fact, it is common practice to use the Dst index as a measure of the magnetic storm intensity (cf. Table 1 of Loewe and Prölss, 1997). A moderate storm has a minimum-Dst between -50 nT to -100 nT, a strong storm has -100 nT > min(Dst) > -200 nT, a severe storm has -200 nT > min(Dst) > -350 nT, and a great storm has min(Dst) < -350 nT.

A geomagnetic storm can generally be split into three distinct phases: the initial, main, and recovery phases. The initial phase is characterized by an enhancement in the Dst index (or in one-minute component SymH index) by 20 to 50 nT in tens of minutes driven by enhancements in the magnetopause currents due to a sudden increase in the pressure. The initial phase is also referred to as a Storm Sudden Commencement (SSC). However, not all geomagnetic storms have an initial phase, and not all sudden increases in Dst or SymH are followed by a geomagnetic storm. The main phase of a geomagnetic storm is identified from a sharp and rapid negative excursion in the Dst index, driven by significant energization of the ring current. The duration of the main phase is typically 2–8 hours. The recovery phase is when Dst changes from its minimum value to its quiet time value as the ring current decays. The recovery phase may last as short as 8 hours or as long as seven days (Walach & Grocott, 2019).
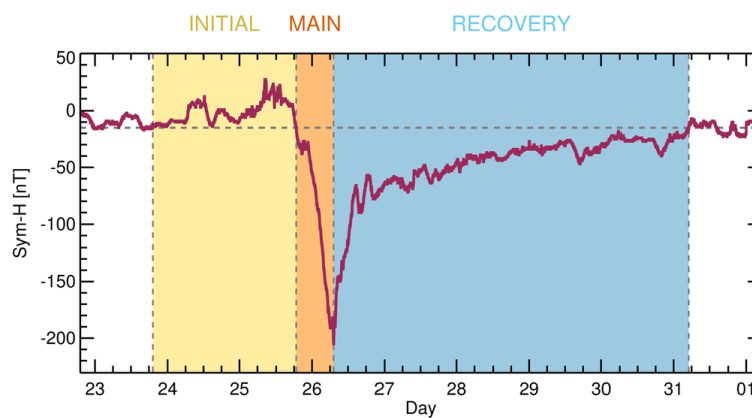
FIGURE 1.12: The Sym-H trace during a geomagnetic storm, where the storm peak occurred at 07:11 UT on August 26, 2018. The colored regions show the phase identification where the initial phase is in yellow, the main phase in orange, and the recovery phase in blue. (Sandhu et al., 2021).

1.4.3   High-Latitude Energy Dissipation: Joule Heating and Auroral Precipitation

So far, we only discussed the low-mid latitude dissipation of energy during the geomagnetic storm. However, one of the most parts of the energy dissipation occurs in high latitude regions. Dayside merging and nightside reconnection produce plasma flow in the ionosphere, which can be intense and steady during a geomagnetic storm. The *flow* means that there is an electric field in Earth's reference frame, and this electric field drives auroral electrojet currents that close the Birkeland currents driven by reconnection. This current dissipates energy in the ionosphere through frictional heating that is generally referred to as **Joule heating**, although actual electromagnetic Joule heating should be calculated in the plasma frame (Vasyliūnas & Song, 2005). However, this important quantity has been challenging to monitor continuously over the entire polar region.

Direct measurements of ionospheric electric fields and conductivities – with rocket-borne instrumentation or with the incoherent scatter Chatanika radar – can only provide Joule heating rates integrated over a small area. Therefore a geomagnetic index such as AE has been used as a first approximation measure of the global Joule heating rates (Baumjohann & Kamide, 1984). The AE index (Nose et al., 2015) is produced at a 1-min cadence using data from up to 12 magnetometer stations at latitudes that correspond to the average location of the auroral oval. The auroral upper index, AU, is defined as the record from the station with the largest positive H-component disturbance. The auroral lower index, AL, is the record from the station with the largest negative H-component

disturbance. The AE index is then the difference between the upper and lower values, AE = AU - AL (Bergin et al., 2020).

SuperMAG now produces SME, an equivalent to AE, at a 1-min cadence (Gjerloev, 2012). SME is the difference between upper (SMU) and lower (SML) indices, that is, SME = SMU - SML. SMU and SML are based on the H-component measured at stations in the latitudes of the auroral oval, with baseline removal carried out. The difference between AE and SME is the number of stations used in their derivation. While AE uses 12 stations, the number of stations used to derive SME increases with time.

The Joule heating rate can be calculated based on doubling the hemispheric rate based on the AE index (Baumjohann & Kamide, 1984; Østgaard, Germany, et al., 2002; Østgaard, Vondrak, et al., 2002) as,

$$U_{JH}(GW) = 0.64AE \, . \tag{1.7}$$

In addition to the Joule heating, solar wind energy can deposit in the auroral ionosphere by precipitating particles. Like the Joule heating, auroral precipitation can be calculated by doubling the hemispheric rate based on the AL index (Baumjohann and Kamide, 1984; Østgaard, Germany, et al., 2002; Østgaard,

Vondrak, et al., 2002) as,

$$U_{AP}(GW) = 2(4.4\sqrt{AL} - 7.6) \,. \qquad\qquad (1.8)$$

Chapter 2

Role of Density in Controlling Energy Transfer into Ionosphere

2.1 Positive Correlation of Solar Wind Density and SME in the Saturation regime

It had long been believed that solar wind density is not a controlling parameter for the auroral electrojets [e.g., Murayama et al. (1980)]. Shue and Kamide (2001) reported two periods in which the solar wind density was strongly correlated with the AL and AU indices. The first period was during southward IMF during the main phase of the geomagnetic storm that occurred January 10, 1997 (figure 2.1). The second period was during strongly northward IMF and density reaching $150 cm^{-3}$ on January 11, 1997 (figure 2.8). However, at that time, the physical origin of these relationships was not well understood. As mentioned in the Introduction, saturation of the ionospheric potential occurs under conditions of low Mach number and large-southward IMF, which means the potential of the

ionosphere becomes relatively intensive to changes in the IMF. Under these conditions, the geoeffective length is proportional to the solar wind density, so that increases in density will result in a greater rate of dayside merging. This results in a correlation between the solar wind density and the intensity of the auroral. Lopez et al. (2004) use the LFM simulation to study January 10 event (Shue & Kamide, 2001) and they find similar behaviour shown in figure 2.2. This work is notable since it showed that MHD simulations could capture this effect for the first time.
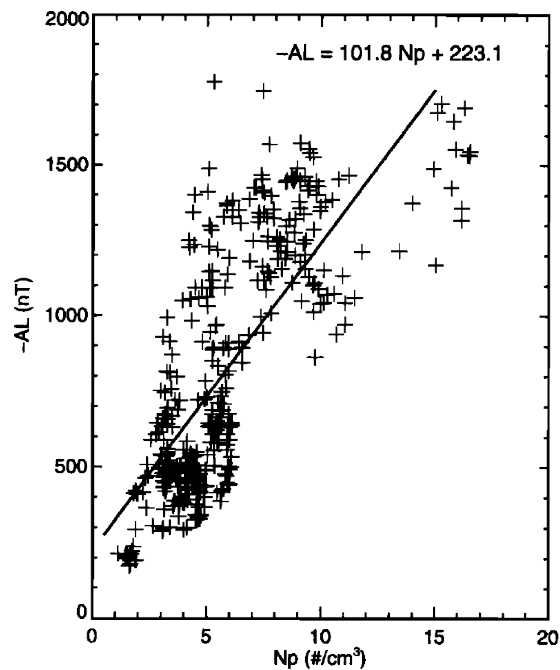
FIGURE 2.1: The correlation coefficient between the AL index and the solar wind density for the event January 10, 1997 from Shue and Kamide (2001, figure 2).

10 January 1997
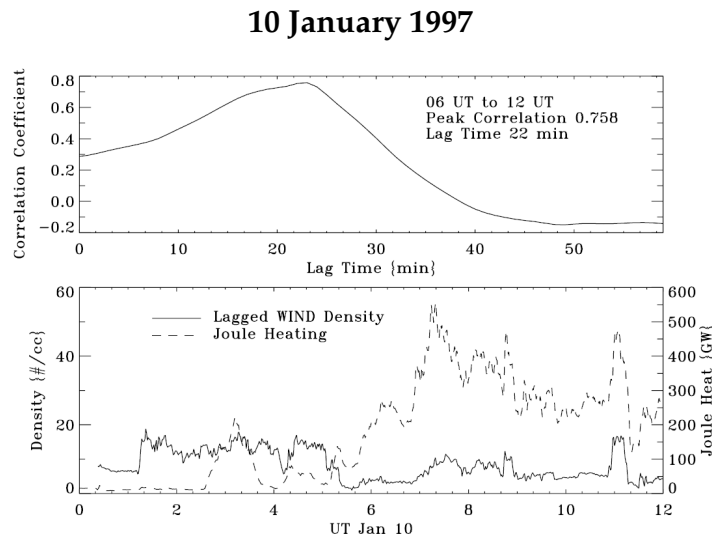
FIGURE 2.2: Lopez et al. (2004) use the LFM simulation to study January 10 event: The bottom panel shows the integrated Joule heating in the northern ionosphere in the simulation along with the solar wind density. The top panel shows the correlation between the solar wind density and the Joule heating for the period 0600 UT to 1200 UT as a function of lag time, where zero lag is the time of solar wind entry onto the grid upstream of the bow shock.

To investigate the effect of the solar wind density on the intensity of the auroral electrojets in the saturation regime, we picked the storms of our storms sample that during their main phase, the solar wind parameters are almost steady, except the density, which changed significantly. In the following, we present two storm events, one with the low Mach number and the other with the regular Mach number. The first storm occurred on June 1, 2013. The main phase of this storm started at 0100 UT and ended at 0900 UT. In this storm, the minimum of Dst^* is -152 nT. We selected the period between 0420-0700 UT to calculate the correlation between SME and the solar wind density. As seen in figure 2.3, during this period, B_z has a significant value and is roughly constant. Mach

number is less than 4, and the solar wind parameters other than density are relatively constant. In the left panel-top of figure 2.4, we can see that the greatest correlation (0.71) occurs when the lagtime between the solar wind data and the SME index is 9 minutes. In the left panel-bottom of figure 2.4, the linear relationship between SME and solar wind density is illustrated.

Since this relationship between solar wind density and SME is because of large-scale Magneto-Hydro-Dynamic (MHD) physics, global MHD models should reproduce results from data. Therefore, to confirm this relationship, we used the Space Weather Modeling Framework (SWMF) simulation for this storm event already done via the Community Coordinated Modeling Center (CCMC). The SWMF simulation combines numerical models of the Inner Heliosphere, Solar Energetic Particles, Global Magnetosphere, Inner Magnetosphere, Radiation Belt, Ionosphere, and Upper Atmosphere into a parallel, high-performance model (Gombosi et al., 2004). Two versions of the SWMF model are used on CCMC. We used the version of v20180525. The relationship between Joule heating and solar wind density is equivalent to the SME-solar wind density relation since Joule heating is a scaled function of SME (see Chapter 3). Thus, we calculated the correlation between solar wind density and the simulated joule heating for this event. As shown in figure 2.4-*right panel*, we can see the same pattern from the SWMF simulation; the joule heating power is highly correlated to the SW density (with correlation coefficient 0.67 considering 5 minutes lagtime).

Solar Wind and SM-Indices during the Event on 1 Jun 2013
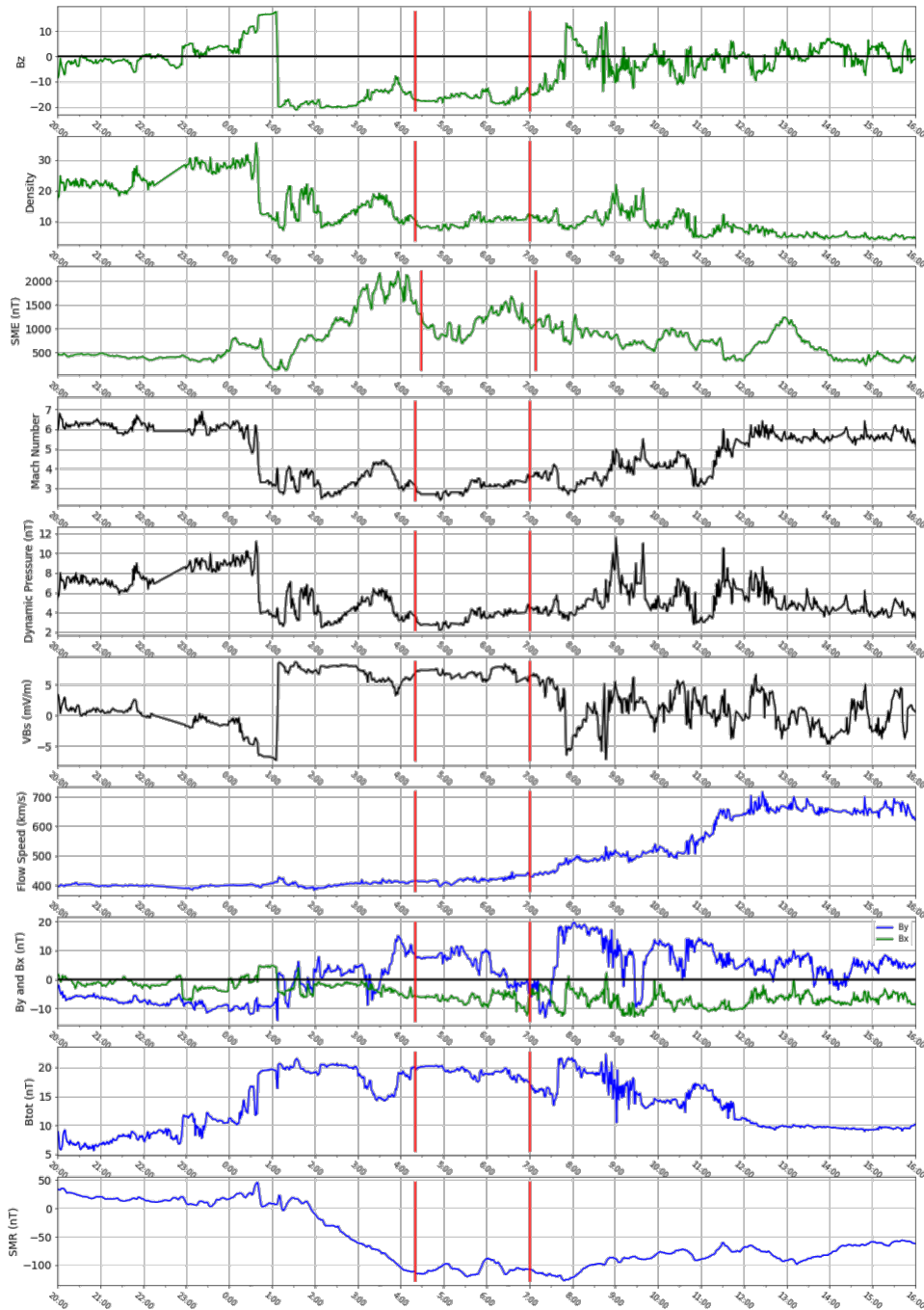
FIGURE 2.3: OMNI and SuperMAG data for the event 1 Jun 2013.
The period between red lines is the selected period for this event.

1 Jun 2013
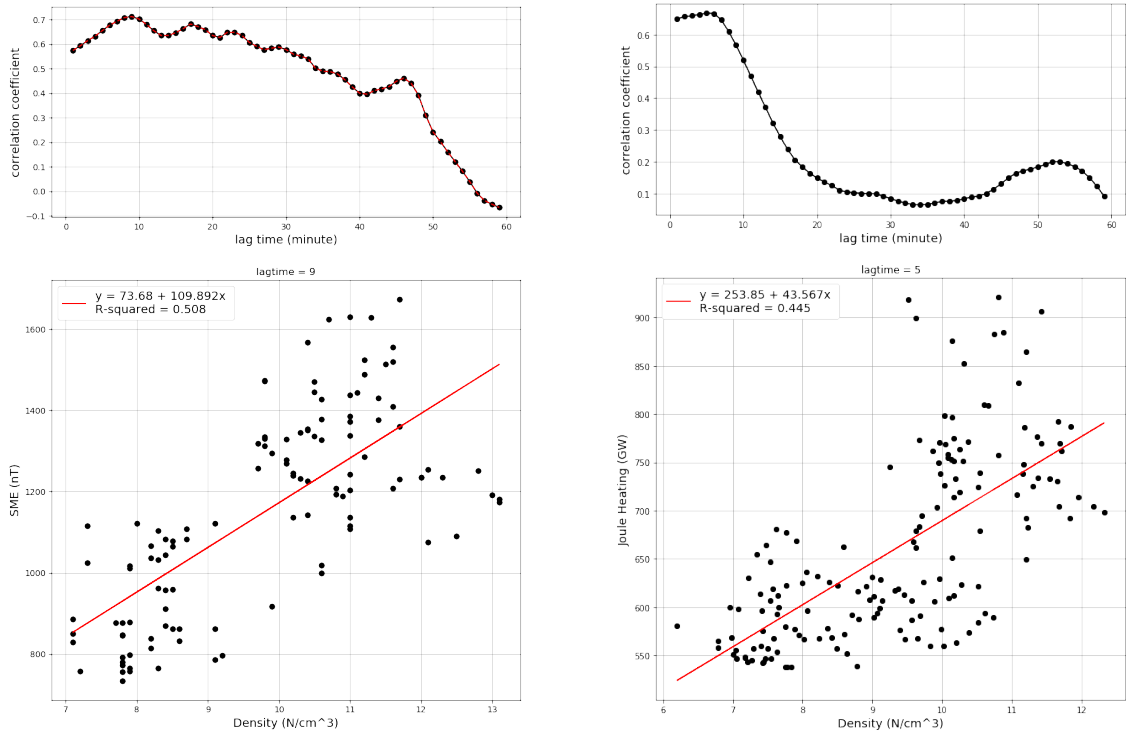
(A) Observation   (B) Simulation

FIGURE 2.4: *Left panel-top:* The correlation coefficient between the SME index and the solar wind density as a function of lagtime. *Left panel-bottom::* The SME index vs. solar wind density for the selected period in the event on 1 Jun 2013.*Right panel-top:* The correlation coefficient between the simulated Joule heating power and the solar wind density as a function of lagtime. *Left panel-bottom::* The the simulated Joule heating vs. solar wind density for the selected period in the event on 1 Jun 2013.

However, the second storm with a regular Mach number happened on December 20, 2015. This is a double storm, and we only consider the first part of

it. The first part has the main phase started at 0400 UT and ended at 1000 UT. The minimum of Dst^* in the first part of this storm is -116 nT. We selected the period between 0610-0810 UT to calculate the correlation between SME and the solar wind density. As it is seen in figure 2.5, during this period, B_z has a large value and is roughly constant, VB_s and total magnitude of B are steady as well, but Mach number has a median value (≈ 6), and it is mostly constant. Thus, this value of Mach number indicates that we are not in the saturation regime. The SME index does not correlate with solar wind density, as it can be seen in figure 2.6. Since the saturation of the potential did not happen, the merging interaction has a significant role in controlling energy transfer into the ionosphere. Based on (Bruntz et al., 2012), during this period, the viscous potential is ≈ 78 kV on average, and the reconnection potential is roughly 160 kV. Since the viscous potential scales like $\sqrt{n}$, there is some dependence on density (for a different reason than discussed with the force-balance model). Since the reconnection potential is higher than the viscous potential and not saturated, there is not a strong correlation between the density and SME.

Solar Wind and SM-Indices during the Event on 20 December 2015

FIGURE 2.5: OMNI and SuperMAG data for the event 20 December 2015. The period between red lines is the selected period for this event.

20 December 2015
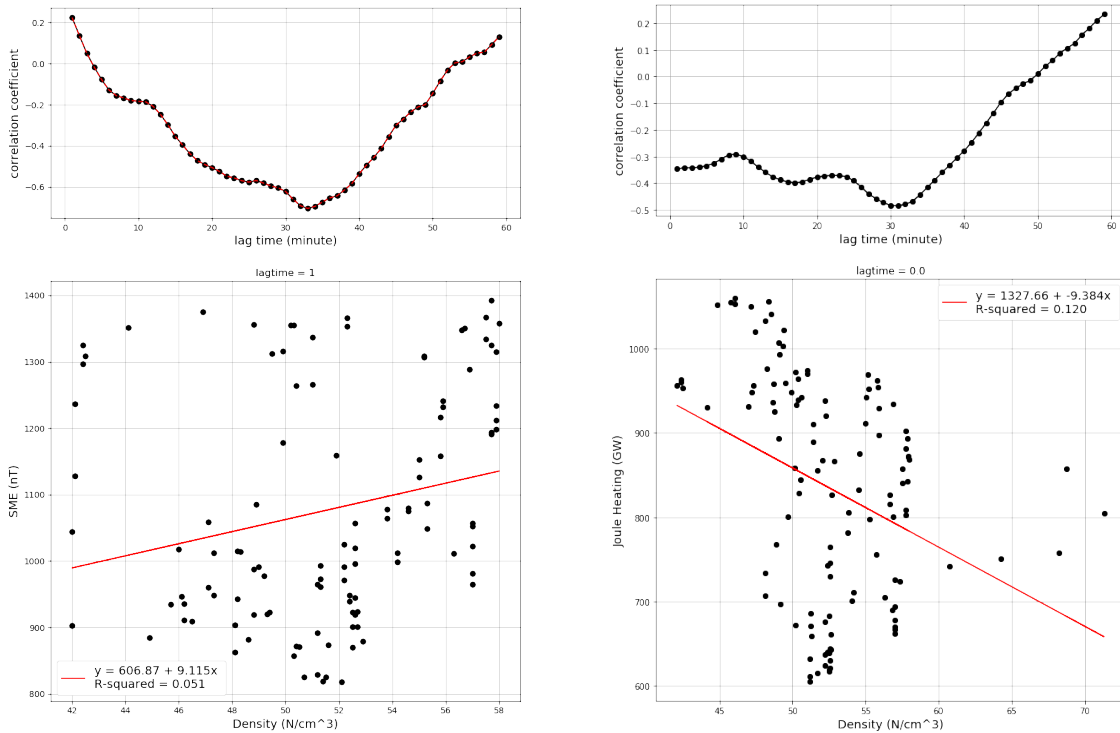
(A) Observation (B) Simulation

FIGURE 2.6: *Left panel-top:* The correlation coefficient between the SME index and the solar wind density as a function of lagtime. *Left panel-bottom::* The SME index vs. solar wind density for the selected period in the event on 20 December 2015.*Right panel-top:* The correlation coefficient between the simulated Joule heating power and the solar wind density as a function of lagtime. *Left panel-bottom::* The the simulated Joule heating vs. solar wind density for the selected period in the event on 20 December 2015.

We study 11 geomagnetic storms similar to the first event presented here. The IMF is large and southward during these storms (summarized in table 2.1).

Also, the Mach number is low. Considering all the events, in figure 2.7, we present the correlation coefficient between the solar wind density and the SME index as a function of the average value of Mach number during the selected period for each event. As can be seen, the correlation coefficient gets larger as the Mach number decreases, indicating that the effect of density is greater. This happens because a lower Mach number leads to a more saturated ionospheric potential; therefore, the intensity of the auroral electrojet mostly depends on the solar wind density rather than the other parameters of the solar wind. This means the variations in the SME index are more correlated to the variations of the solar wind density. We can conclude that during storms with low Mach number, the solar wind density is an important control factor for the energy input into the ionosphere.

TABLE 2.1: List of Storm Event Used in This Study.

Date	Time of Main Phase	min Dst^*	Selected Period
10 January 1997	06-12 UT	-87 nT	0600-1200 UT
20 August 1998	07-20 UT	-84 nT	1000-1400 UT
13 November 1998	05-22 UT	-150 nT	0700-0930 UT
28 Feb.-1 March 1999	17-01 UT	-122 nT	1800-2030 UT
13 November 1999	12-23 UT	-122 nT	1800-2100 UT
14 October 2000	02-15 UT	-127 nT	1100-1420 UT
3 October 2001	06-15 UT	-187 nT	0915-1115 UT
26-27 June 2004	22-03 UT	-142 nT	0900-1250 UT
30 May 2005	06-14 UT	-138 nT	0715-1015 UT
1 June 2013	01-09 UT	-152 nT	0420-0700 UT
27 August 2014	03-19 UT	-103 nT	0930-1330 UT
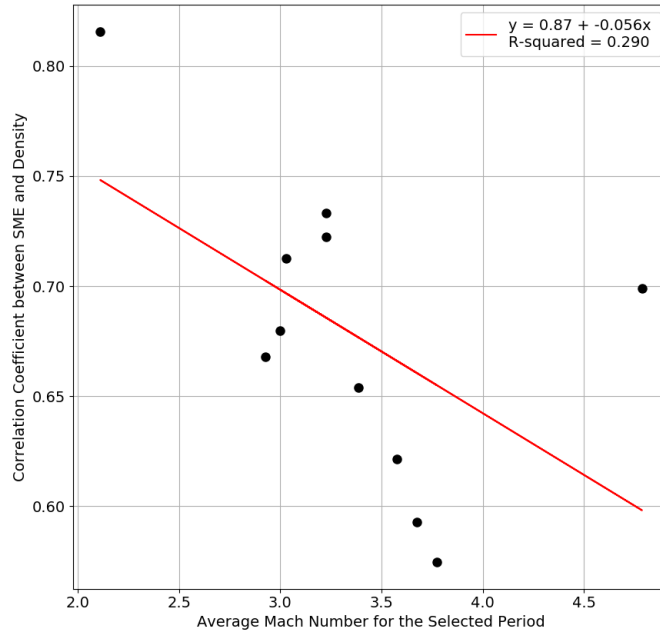
FIGURE 2.7: The correlation coefficient between the SME index and the solar wind density in terms of the average Mach number for the selected period of each event. The red line is the linear fit to data which shows lower Mach number leads to a stronger correlation.

2.2 Positive Correlation of Solar Wind Density and SME in Viscous-Dominated Regime

As discussed in Chapter 1, magnetic reconnection and viscous-like interaction are two processes that contribute to the ionospheric potential (Axford & Hines, 1961; Dungey, 1961). Several studies attempt to formulate the changes in the ionospheric potential due to the viscous interaction. Bruntz et al. (2012) used the Lyon-Fedder-Mobarry (LFM) Magneto-Hydro-Dynamic (MHD) simulation

and found that viscous potential in LFM can be predicted using the formula:

$$\phi_V = \frac{\mu}{\gamma}\sqrt{n}V_x^{1.33}\,,\qquad(2.1)$$

where n is the solar wind density, V_x is the flow speed in the x-direction, μ is 0.00431, and the scaling factor $\gamma = 1.54$. This equation is consistent with other studies especially Newell et al. (2008).

In most cases, the primary driver of the ionospheric potential is reconnection. Still, in the case of northward IMF, since the reconnection regions are limited, the changes of the ionospheric potential caused by the viscous interaction can be greater/comparable to the reconnection-driven potential. On the other hand, northward IMF also weakens the viscous interaction (Bhattarai & Lopez, 2013). As described above, the viscous interaction is based on the momentum transfer of the anti-sunward magnetosheath flow into the flow inside the magnetosphere. But the northward merging produces the anti-sunward flow in the magnetosphere, decreasing the shear velocity and hence the viscous interaction between this flow and the flow in the magnetosheath.

In the second event in the Shue and Kamide (2001) paper with the northward IMF (January 11, 1997, shown in figure 2.8), the relationship between the solar wind density and the AU index could be the result of the viscous-like interaction and/or the saturation of potential, since the IMF is large. The values of the solar wind density were so great that an estimate of the potential produced by the viscous-like interaction (Bruntz et al., 2012) show that it would have been the

most significant contributor to energy transfer for the solar wind, leading to the observed correlation. Thus, the density correlations with the auroral electrojets in the two periods identified by Shue and Kamide (2001) were driven by very different physics.
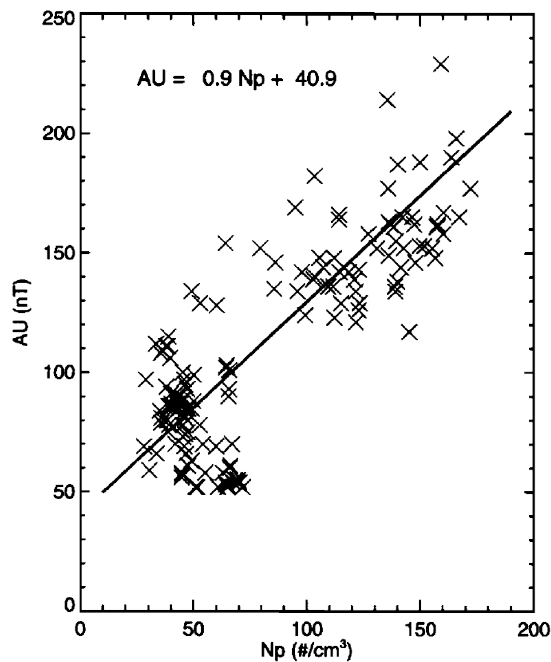
FIGURE 2.8: The correlation coefficient between the the AU index and the solar wind density for the event January 11, 1997 Shue and Kamide (2001, figure 2).

To investigate the role of solar wind density during the viscous-dominated events, we find an event with the *small* northward IMF and high Magnetosoinc Mach number to avoid being in the saturation regime (Lopez et al., 2010). This event happened on September 29, 1996. We selected 3 hours between 0730 UT to 1030 UT. As seen in the figure 2.9, during this period, IMF is mostly northward,

but there are some moments when it turned southward with magnitudes less than -1 nT. These changes in the sign of the IMF do not matter here since SymH data does not show any evidence for the reconnection process. In the selected period, the Mach number starts with the high value, 7.5, this value increases to about 9, and then it goes back to 6.5.

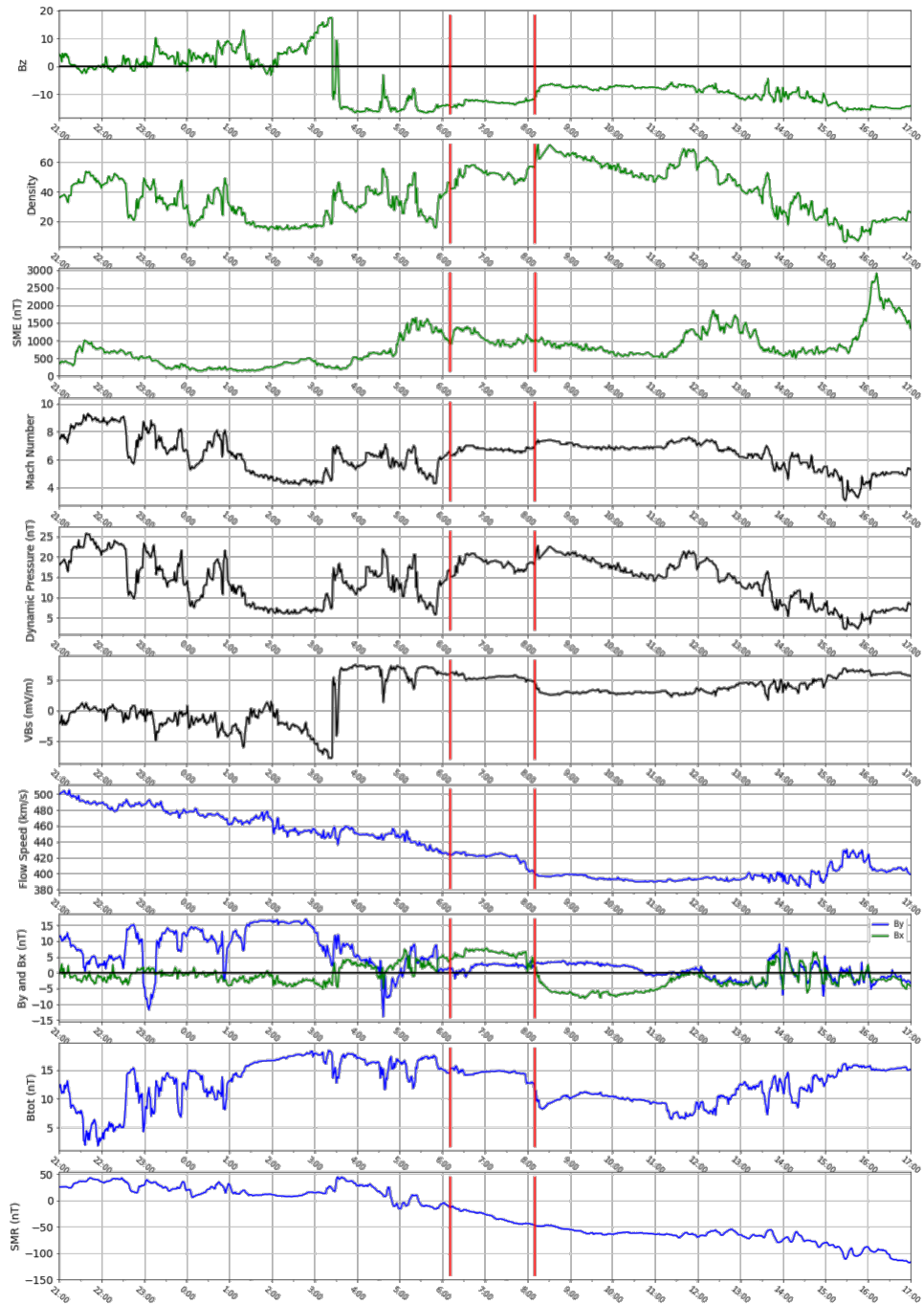**Solar Wind and SM-Indices during the Event on 29 September 1996**
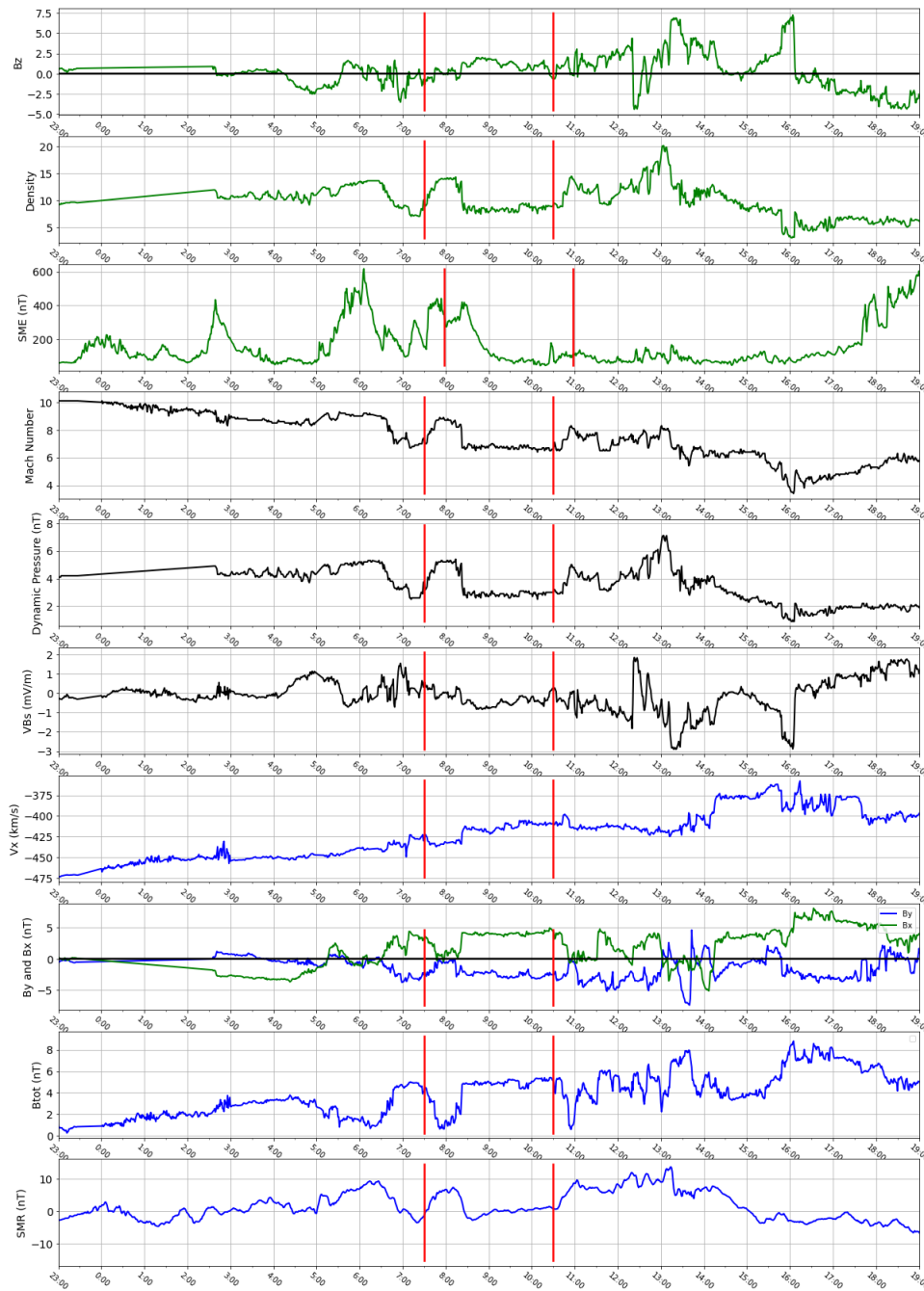
FIGURE 2.9: OMNI and SuperMAG data for the event 29 September 1996. The period between red lines is the selected period for this event.

For this event, we also look at data from DSMP F13, which crossed the southern polar cap from dawn to dusk during the period of interest in this event. The DMSP (Defense Meteorological Satellite Program) data are provided by the CEDAR Madrigal database (http://cedar.openmadrigal.org). The velocity of the plasma is illustrated in the fourth panel (from top) of the figure 2.10. The horizontal component of the velocity is the cross-track plasma flow, where a positive sign means the flow is sunward. Around 0918 UT (when DMSP F13 was at -73.6 MLAT and 3.9 MLT), the spacecraft crossed a Region-I type plasma convection cell (sunward at low latitude, anti-sunward at higher latitude). Since the value of the northward IMF is small in this event, this convection cell seen in the figure must be due to the viscous-like interaction, and the large flow speeds in the cell are consistent with a period in which the viscous interaction was dominant. There is a small reverse convection flow at around 0922, which shows the reverse cell convection during this event, coincident with the magnetosheath-like plasma (top panel) that is the signature of dayside merging during the northward IMF Dungey cycle, as shown in figure 1.7.
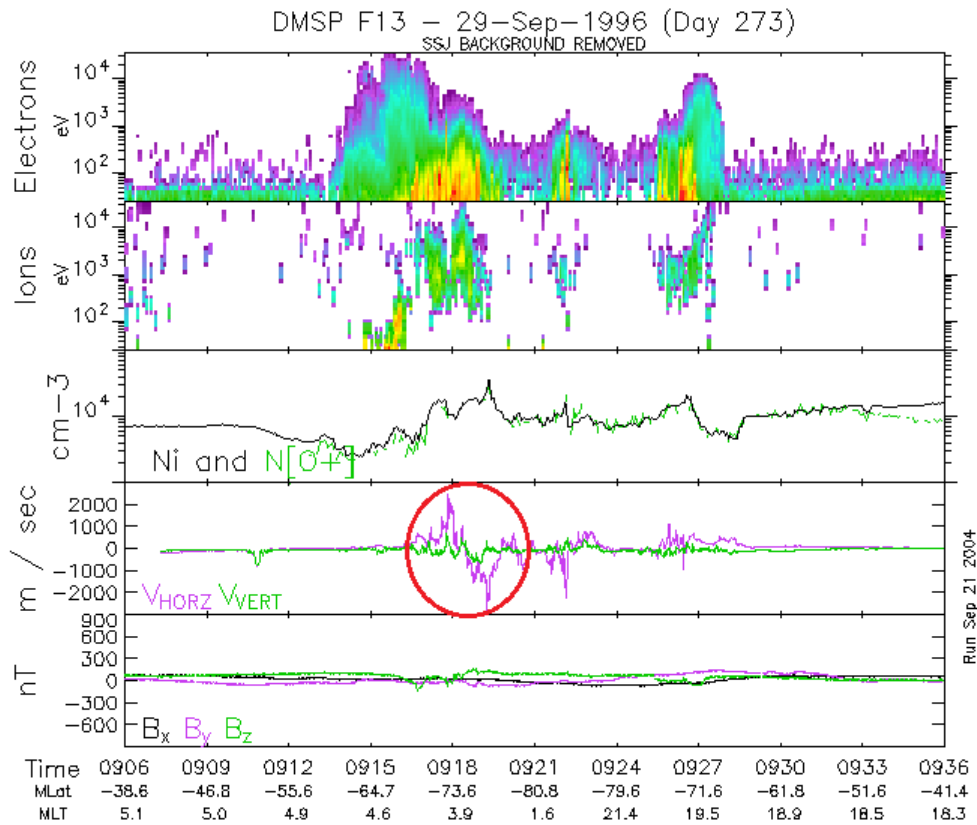
FIGURE 2.10: The circular pattern of the plasma flow during the
event 29 Septemeber 1996 shown in the red circle using DMSP data.

As seen in figure 2.11-*left panel*, the lagtime between the SME index and the
solar wind density is 28 minutes, corresponding to the greatest correlation co-
efficient between SME Index and solar wind density, which is ≈ 0.9. In figure
2.11-*right panel*, the viscous potential is calculated based on empirical formula
introduced by Bruntz et al. (2012) (equation (2.1)). As seen in this example, in
the viscous-dominated events, the solar density and the SME index are highly
correlated, thus increasing the density leads to the increase of the ionospheric
potential via the viscous interaction.

29 September 1996
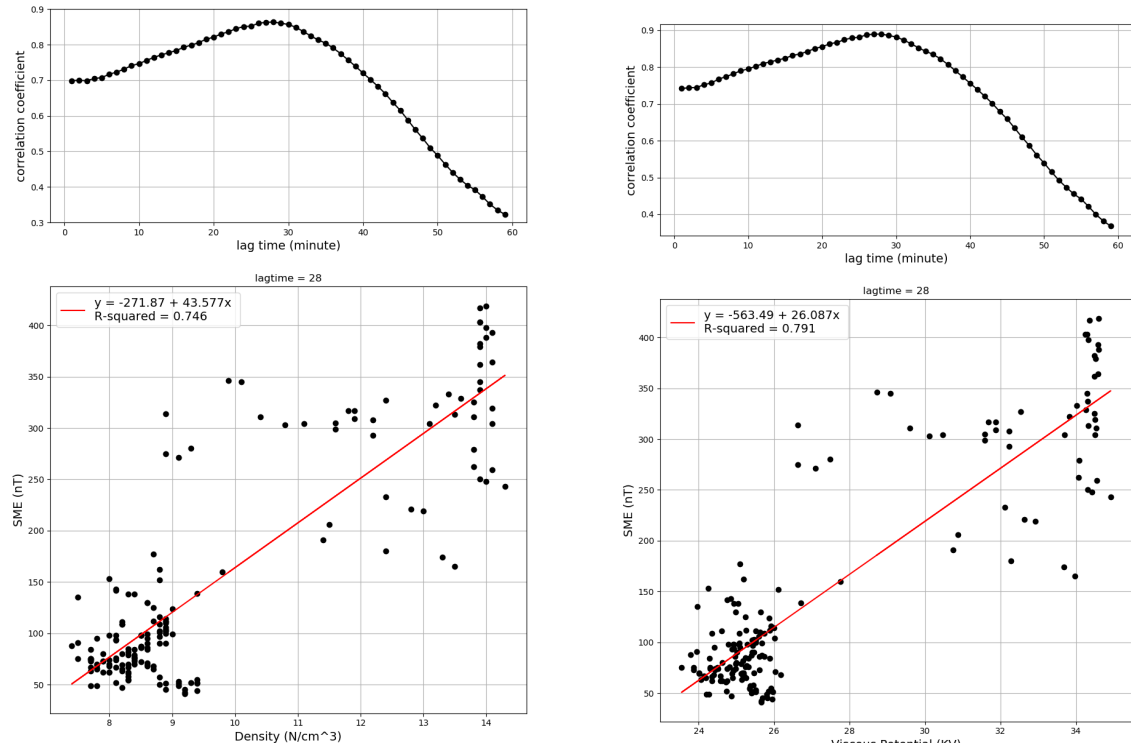
FIGURE 2.11: Event: 29 September 1996: *Left-top:* The correlation coefficient between the SME index and the SW density in terms of time shift between data. *Left-bottom:* The SME index as a function of SW density considering the 28 minutes lagtime. *Right-top:* The correlation coefficient between the SME index and the viscous potential in terms of time shift between data.*Left-bottom:* The SME index as a function of the viscous potential considering the 28 minutes lagtime.

For greater northward IMF, the dayside reconnection process also produces the convection cells so that their orientation opposes the orientation of the convection cells produced via viscous interaction. As a result, there is a 4-cell pattern in the ionosphere, making the situation more complicated than a viscous-dominated period. Bhattarai and Lopez (2013) used LFM simulations and showed

that for the periods of northward IMF but not viciously dominated, increasing B_z results in the greater ionospheric potential until it reaches the saturation regime as discussed in Chapter 1. Therefore, for the periods of moderate northward IMF, the IMF has the main role in the intensity of the auroral electrojets, and solar wind density is not an important factor in enhancing this intensity.

Chapter 3

Energy Dissipation during Magnetic Storms in terms of Solar Wind Magnetosonic Mach Number

3.1 Selection of Storms

A starting point for the studies concerning energy dissipation and the roles of solar wind parameters during geomagnetic storms is to make a comprehensive sample of storms. Toward this goal, we use the Dst index provided by the World Data Center for Geomagnetism, Kyoto (http://wdc.kugi.kyoto-u.ac.jp/dstdir/). For the derivation of the Dst index, this center uses four magnetic observatories located at Hermanus, Kakioka, Honolulu, and San Juan. The coordinates of the observatories are given in Table 1, and a map of the network is given in 3.1. These observatories were chosen on the basis of the quality of observation and because their locations are sufficiently distant from the auroral and equatorial electrojets and that they are distributed in longitude as evenly as

possible.
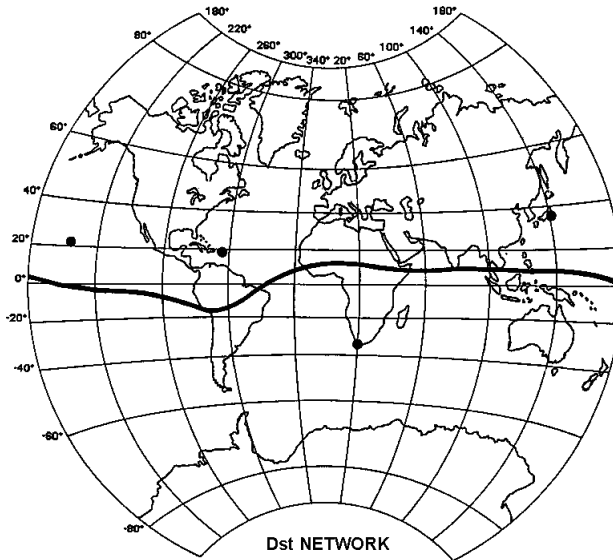
FIGURE 3.1: The Dst Network. Credit WDC website

By writing a **Python** script to capture a sudden decrease in the Dst index, we find 314 magnetic storms with the Dst index ≤ -50 nT, happened between the years of 2000-2020. The full list and information of the main phase of the storms are provided in Appendix A. Then, we calculated the Dst^* index using (1.4) and used this index for the rest of this study. In the next step, we collect the solar wind data during the main phase of each storm using 1-minute OMNI data provided by CDAWeb (https://cdaweb.gsfc.nasa.gov/index.html/). The statistics of the storms in our sample is provided through 3.2-3.4.
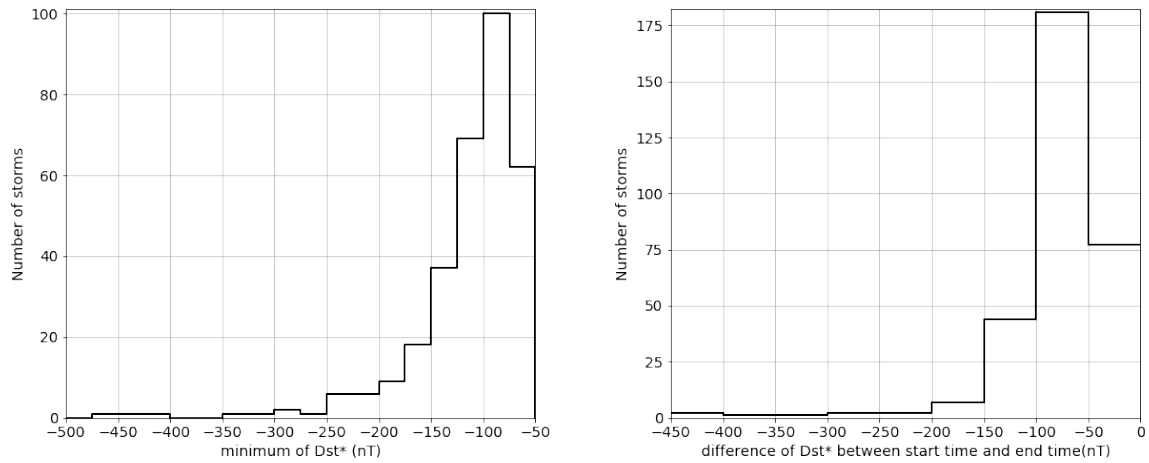
FIGURE 3.2: *Left:* Histogram of number of storms in terms of the minimum value of *Dst**. *Right:* Histogram of number of storms in terms of difference between *Dst** of the begining and ending of the main phase of storms.
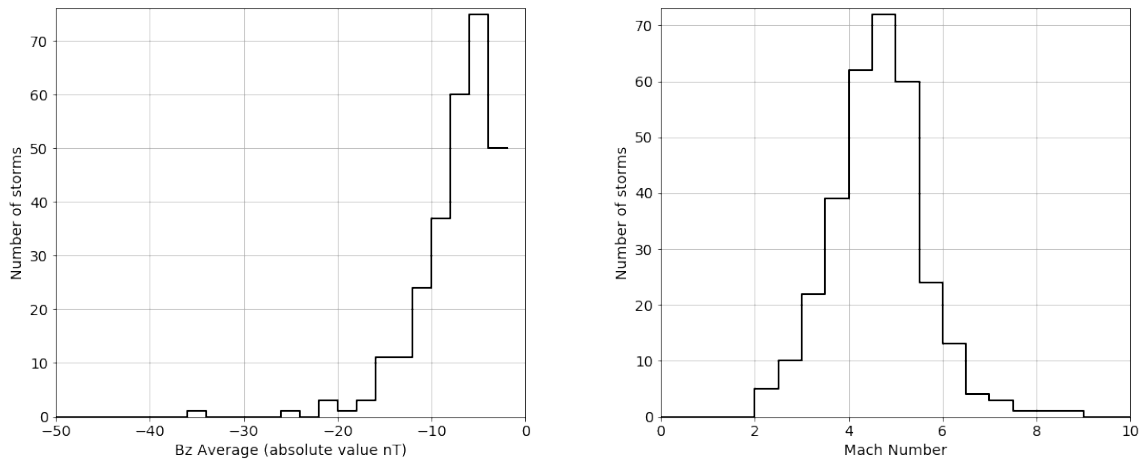
FIGURE 3.3: *Left:* Histogram of number of storms in terms of IMF-z component-averaged through main phase. *Right:* Histogram of number of storms in terms of Mach number-averaged through main phase.
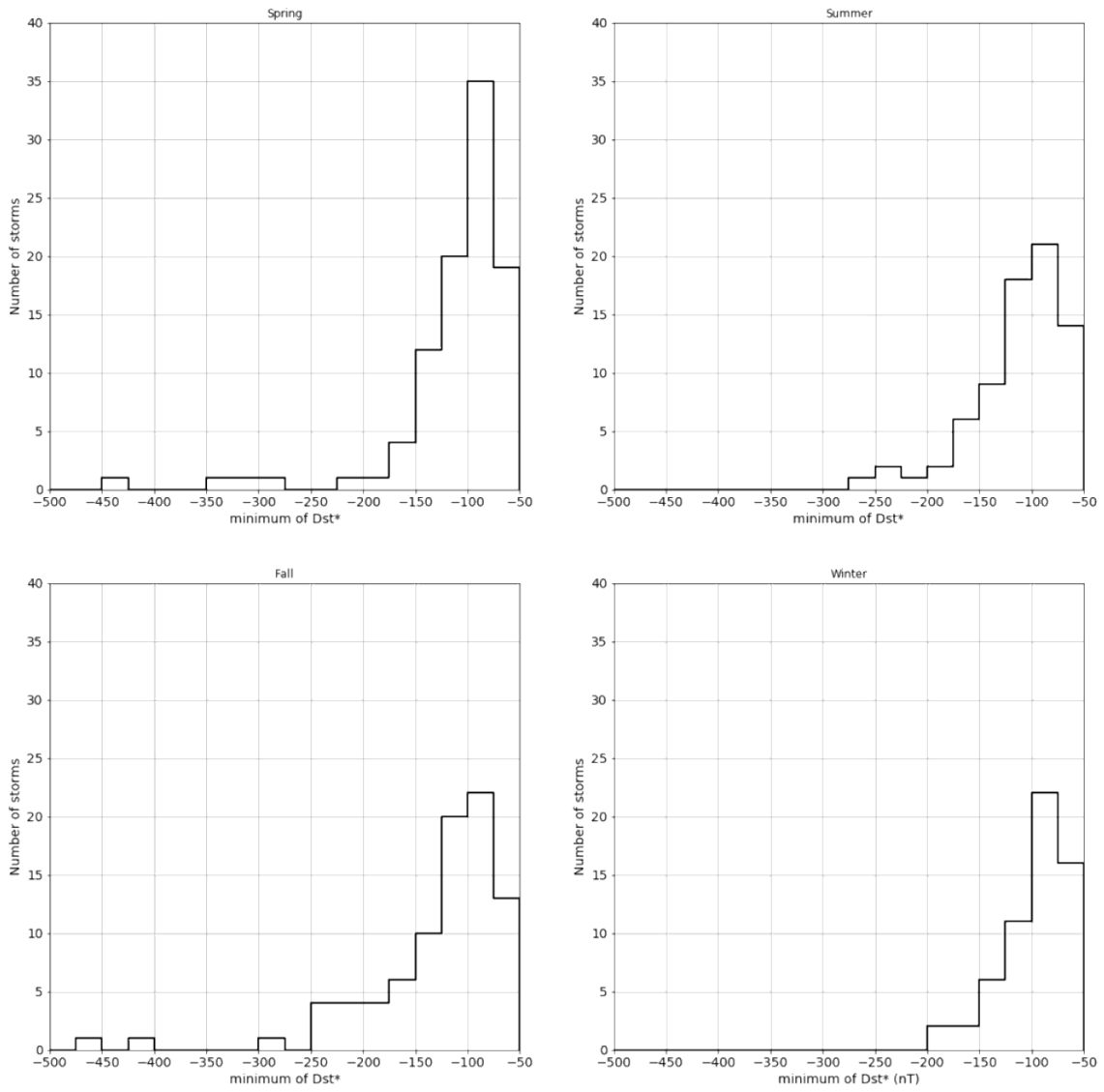
FIGURE 3.4: Number of storms in terms of minumum of *Dst** in
different seasons.

3.2 Correlation between Dst^* and the Ionospheric Power for Different Values of Mach Number

As discussed in Chapter 1, under the condition of low Mach number and high IMF, the ionospheric potential saturates. However, the ring current injection rate does not saturate (Russell et al., 2001). Lopez et al. (2009) argued that the reconnection region moves closer to Earth for higher values of solar wind IMF so that the volume per unit magnetic flux in the closed field line region is less. Thus, the flux tubes coming from a reconnection region can penetrate deeper into the inner magnetosphere. In other words, the injection of particles into the inner magnetosphere produces more energization, and the ring current energy content, hence Dst, continues to be dependent on the magnitude of the IMF. Therefore, one can conclude that under the condition of low Mach number solar wind, the ring current (and so, the Dst Index) continues to respond to the changes of the magnitude of the southward component of the IMF. However, the potential of the polar cap and consequently the auroral electrojet intensity do not continue to respond strongly to IMF variations when the $\vec{J} \times \vec{B}$ term (in (1.2)) becomes dominant in regulating the reconnection potential. Therefore, using the Dst index can be a misleading indicator of the strength of the geomagnetic storms under these conditions.

To investigate the relationship between the energy dissipated in the polar ionosphere and the Dst index, we analyze 314 magnetic storms with $Dst^* \leq -50$ nT for the period between 2000 and 2020. Using the 1-min data from SuperMag

for the SME index and the 1-hr solar wind data from OMNI, we estimate the energy dissipated in the ring current, the Joule heating, and the auroral particle precipitation for each storm. For this study, we only estimate the energy involved in the storm's main phase. To eliminate the influence of the lagtime in the study of the solar wind data and geomagnetic indices, we consider Dst rather than SYM-H as Dst is measured hourly while SYM-H is a 1-minute data. This is important since the lagtime between solar wind data and the geomagnetic indices is about 20 to 35 minutes (Maggiolo et al., 2017), which has a significant effect on using 1-min data. In addition, O'Brien and McPherron (2000) used Dst rather than SYM-H, and to use those results, we need to use the same index that they used to derive the formula.

As discussed by Burton et al. (1975), the changes in the ring current energy content (hence the changes in the Dst^*) is comprised of two terms: the injection term and the proportional loss of the energetic particles,

$$\frac{dDst^*}{dt} = Q(t) - \frac{Dst^*}{\tau} \tag{3.1}$$

[where τ is the decay time. Empirical studies have been done to determine the decay time (Lu et al., 1998; Mac-Mahon & Gonzalez, 1997; O'Brien & McPherron, 2000; Prigancová & Feldstein, 1992; Valdivia et al., 1996). In this paper, we consider τ as described by O'Brien and McPherron (2000),

$$\tau(hrs) = 2.4 \exp \frac{9.74}{4.69 + VB_s} \tag{3.2}$$

where V is the solar wind speed, and B_s is the southward IMF component, assuming it is zero if B_z was northward. Thus, we estimate the ring current injection rate, the Joule heating, and the auroral precipitation from equations (3.1), (1.7), and (1.8), respectively.
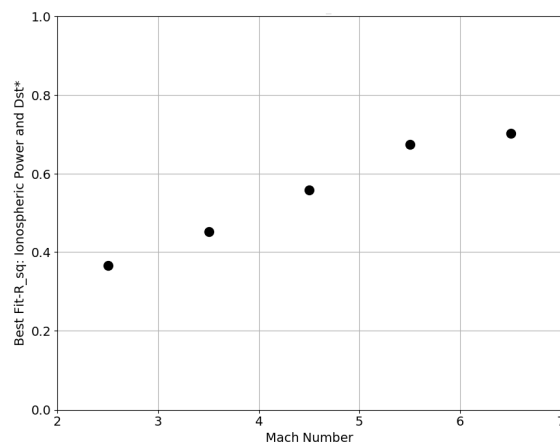
FIGURE 3.5: The R^2 for the best fit of the ionospheric power as a function of the $Dst*$ index for different ranges of averaged Mach number. The power and the Mach number are all the main phase-averaged values of the geomagnetic storms.

We categorized the storms based on the average value of the magnetosonic Mach number in the main phase of each storm. For each category, we calculated the correlation between the Dst* index and the energy dissipated via the ring current injection rate, the Joule heating, and the auroral precipitation. Moreover, for each category, we found the best linear fit for these three kinds of energy dissipation as a function of Dst*. As illustrated in 3.5, a lower Mach number leads to a smaller correlation for the ionospheric power. But the ring current injection rate does not show this behavior. As expected, this pattern can also be seen in

3.6, where the correlation between Dst* and the maximum of the ionospheric power is represented. Based on these figures, we can conclude that for a smaller value of Mach number, the dependence of the amount of ionospheric Joule heating and auroral dissipation on storm size as defined by Dst^* is less, so that for the lowest Mach number storms, the ionospheric dissipation is essentially independent of Dst^*. This is related to the saturation of the ionospheric potential. As the voltage imposed across the ionosphere saturates, the ionospheric currents and the joule heating, and the auroral particle precipitation also saturate. However, since Dst* does not saturate, it continues to respond to the magnitude of the southward IMF while the ionospheric power does not. Other factors besides the magnitude of the IMF control the saturation value of the potential and hence the amount of ionospheric dissipation. Also, the fraction of the total energy which dissipated in the ring current is less than the fraction that dissipated in the ionosphere. In 3.7, the fraction of energy dissipated in the ring current as a function of the main phase-averaged Mach number is presented. As seen, this fraction is almost less than 1/3 of the total energy transferred to the magnetosphere-ionosphere system. Also, it increases for lower values of the Mach number since the ring current injection rate continues to increase with IMF Bz while the polar cap currents saturate.
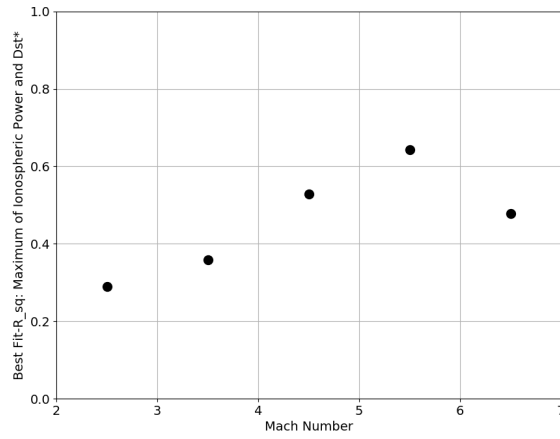
FIGURE 3.6: The R^2 for the best fit of the maximum of the ionospheric power (during the main phase,) as a function of the Dst^* index for different ranges of averaged Mach number.
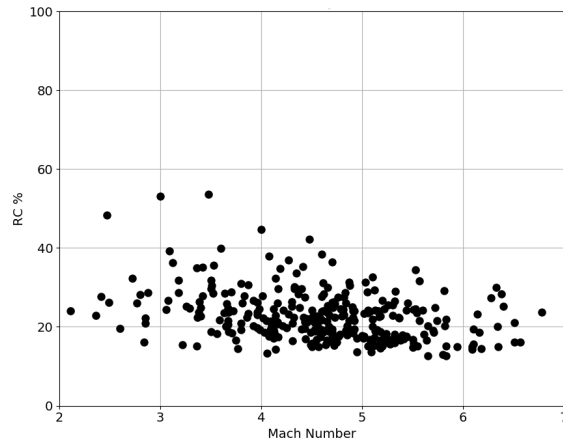
FIGURE 3.7: The percentage of the energy dissipated in the ring current as a function of averaged Mach number for all 314 storms.

3.3 Correlation between Geoeffectiveness and Ionospheric Indices for Different Values of Mach Number

Geoeffectiveness refers to the efficiency of energy coupling from the solar wind into the magnetosphere. It has been shown that the geoeffectiveness is correlated with the Dst index and thus the ring current injection rate. As discussed before, during storms with a low Mach number, the saturation of the potential occurs, so that further increases in IMF magnitude divert more flow away from the merging line, decreasing the geoeffective length and limiting the global merging rate. However, as mentioned earlier, the fact that the ring current injection rate does not saturate indicates that for the low Mach number storm events, the geoeffectiveness is less correlated to the ionospheric potential compared with high Mach number events. To show this, in this section, we investigate the relationship between the ionospheric current and the geoeffectivness during magnetic storms.

To define the geoeefctiveness, we should have accurate measurements of the total amount of energy entering the magnetosphere from the solar wind. Although this is not a simple task, different parameters have been defined to estimate the energy input to the magnetosphere. One of them is the ϵ parameter which is defined in (SI units) as

$$\epsilon = (\frac{4\pi}{\mu_0})vB^2\sin^4(\theta/2)l_0^2 \, , \tag{3.3}$$

where v is the solar wind speed, B is the magnitude of the IMF, l_0 is a characteristic length scale representing the coupling area available for solar wind-magnetosphere interactions, usually approximated as $7R_E$ (Perreault & Akasofu, 1978), μ_0 is the permeability of free space, and θ is defined as

$$\tan^{-1}(|B_Y|/B_Z) . \tag{3.4}$$

In fact, ϵ parameter is a measure of the Poynting flux in the solar wind over the magnetospheric collecting area (Turner et al., 2006). If the IMF was purely southward, the term $\sin^4(\theta/2)$ reaches its maximum value, and therefore the energy coupling of solar wind and magnetosphere increases significantly. However, this term ($\sin^4(\theta/2)$) can also enhance energy coupling during the northward IMF. Furthermore, the l_0^2 term in this equation is a constant length scale, while the magnetopause area is known to vary with solar wind conditions (MacMahon & Gonzalez, 1997). Therefore, the ϵ parameter does not exactly quantify the energy coupling of solar wind and the magnetosphere, but rather, it shows an *estimation* of the energy dissipated into the magnetosphere.

In addition to ϵ, there are some other parameters to quantify the energy coupling somehow. For instance, one can parameterize solar wind energy input with vB_S, where v is the solar wind velocity, and B_S is the southward component of the IMF (O'Brien & McPherron, 2000). Another one, defined by Bargatze et al. (1985) which is similar to ϵ in terms of having the $\sin^4(\theta/2)$, but it is a more complex equation.

In this section, we study the relationship between geoeffectiveness, ϵ, and the SME index. Both data are provided by SuperMag collaborators and can be found at http://supermag.jhuapl.edu/indices/ (Gjerloev, 2012). For the first step of studying 314 storms that we have in our sample, we calculate the best linear fit for the SME index as a function of ϵ during the main phase of each storm. Then, similar to the previous section, we categorized the storms based on the average value of the magnetosonic Mach number in the main phase of them. After that, for each category, we calculated the average of the slopes of the linear fits. As illustrated in figure 3.8, as the averaged-Mach number increases, the average of the slopes also increases.
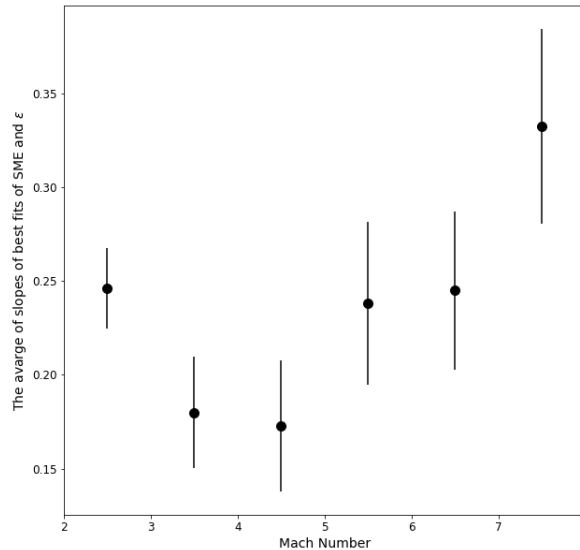
FIGURE 3.8: The average slopes of the best fits of the SME index as a function of the ϵ for different ranges of averaged Mach number.

The other way to see such behavior is by using the averaged SME index. For each storm, we calculate the average value of the SME index and ϵ during

the main phase. Then, similar to the past, for each category of storms (based on the average value of the Mach number), we calculate the correlation of the averaged-SME index and the averaged-ϵ. Figures 3.9- 3.11 shows the linear relationship between $< SME >$ and $< \epsilon >$. As also illustrated in figure 3.12, for the higher Mach number, the correlation coefficient is greater. This result is consistent with the theory of force-balance. As the Mach number decreases, the geoeffective length gets shorter; hence, the ionospheric current and the geoeffectiveness are less correlated 3.12. In other words, the ionospheric potential dependency on geoeffectiveness is smaller 3.8.
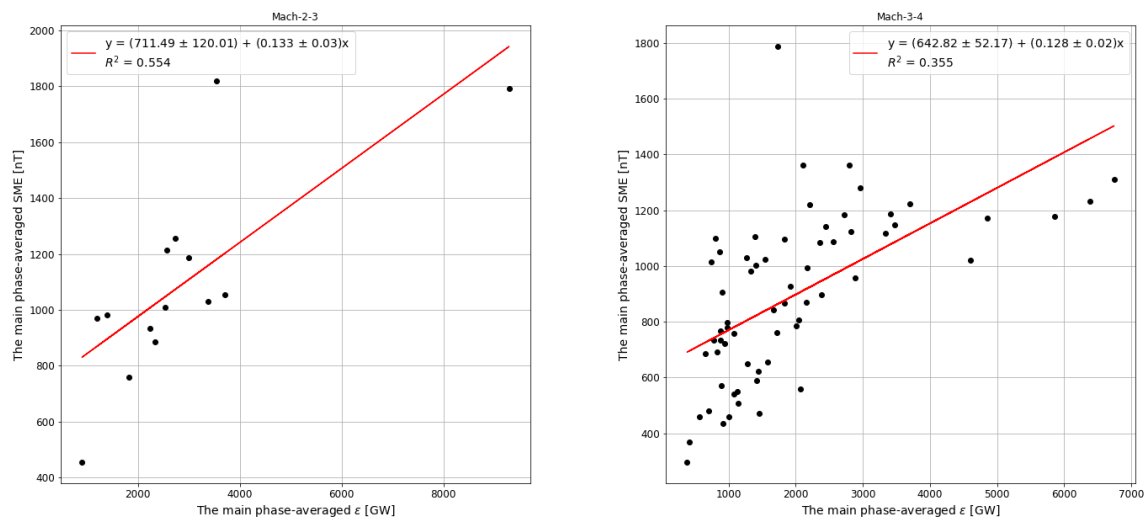
FIGURE 3.9: The best linear fit of the averaged-SME index and the averaged-ϵ for events with the Mach number: *left*-between 2-3 *right*- between 3-4.
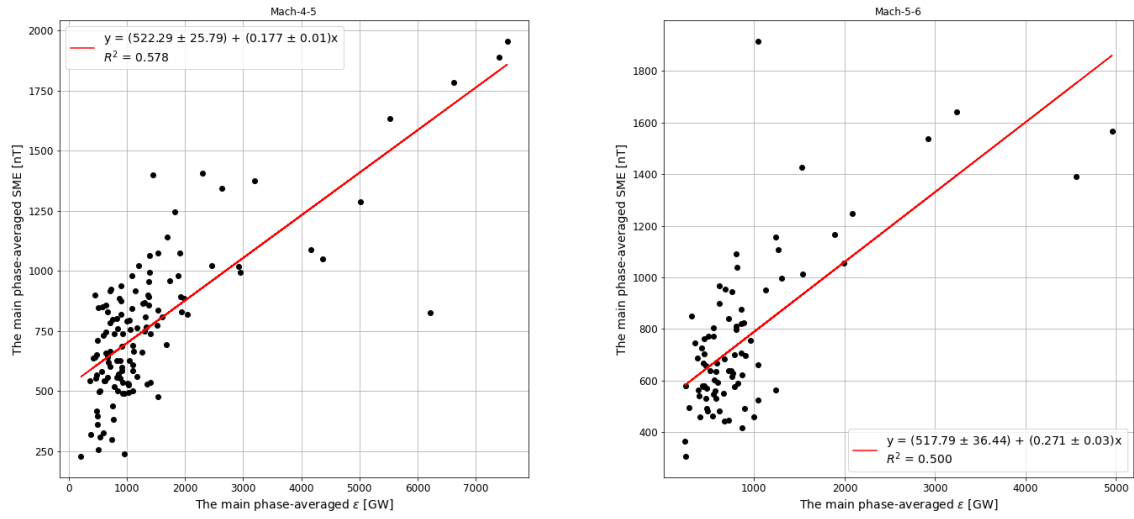
FIGURE 3.10: The best linear fit of the averaged-SME index and the averaged-ϵ for events with the Mach number: *left*-between 4-5 *right*- between 5-6.
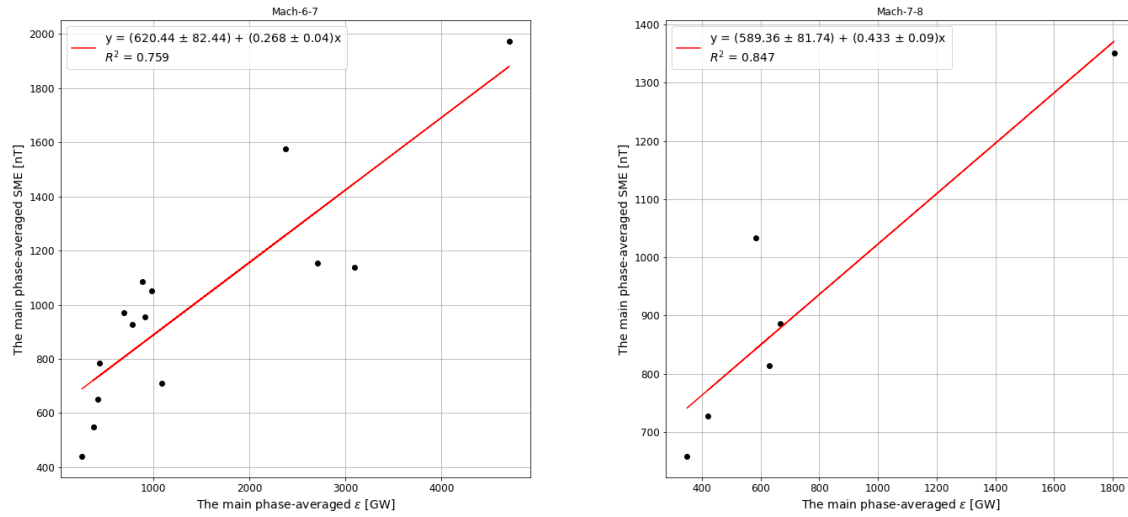
FIGURE 3.11: The best linear fit of the averaged-SME index and the averaged-ϵ for events with the Mach number: *left*-between 6-7 *right*- between 7-8.
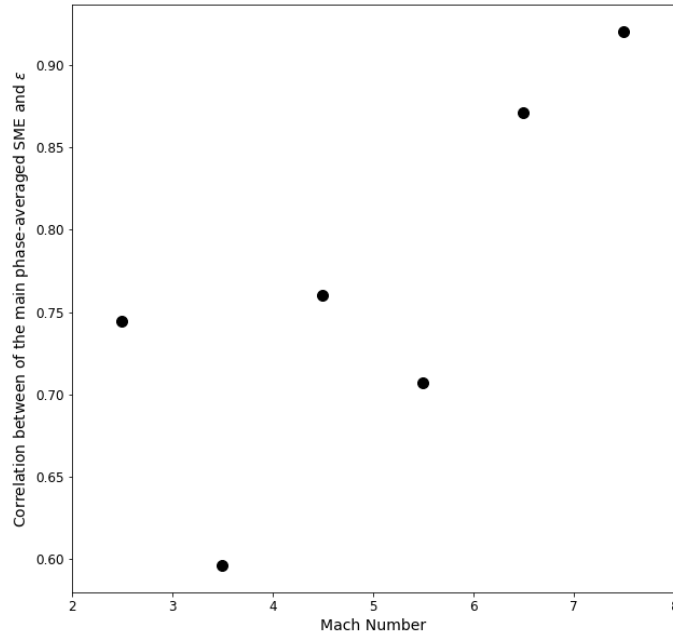
FIGURE 3.12: The correlation coefficient of the averaged-SME and
the averaged-ϵ for different ranges of averaged Mach number.

Another way to study the geoeefectiveness of solar wind is by looking at the ratio of energy dissipated into the ring current per VB_s of the solar wind, called α ($\alpha = RC/VB_s$). We can also study the ratio of energy dissipated to the ionosphere per VB_s, $\alpha_{ionospheric} = (JH + AP)/VB_s$ where JH is the Joule heating and AP is the energy dissipated through auroral precipitation. Hence, for each storm in our sample, we calculate the main-phased averaged of the energy dissipated in the ring current and in the ionosphere (JH + AP). Then, divided by the average of VB_s during the main phase of the storm. Figures 3.13-3.16 show the histograms of the parameters α and $\alpha_{ionospheric}$ in different seasons. There does not seem to be seasonal dependence, even though for the ionosphere one might expect a dependence due to the seasonal changes in the conductivity.
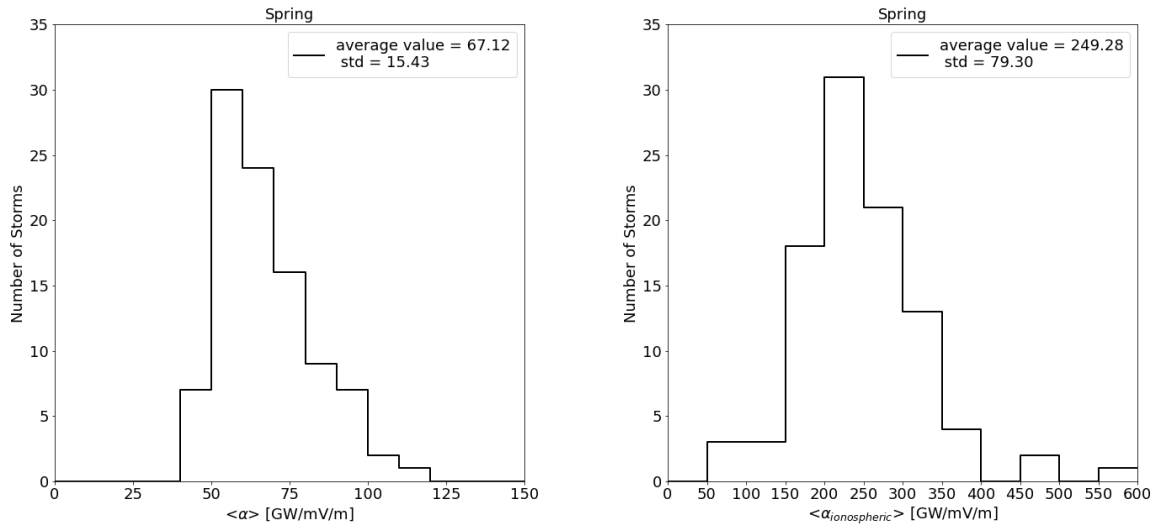
FIGURE 3.13: Histogram of number of storms in terms of the main phase averaged value of *left: α* and *right: α$_{ionospheric}$* in Spring.
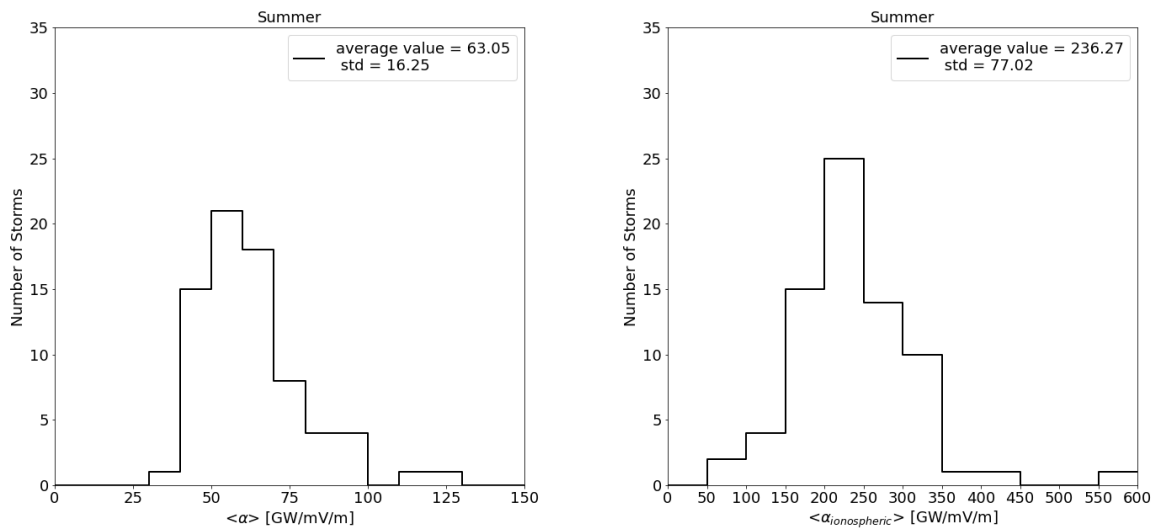
FIGURE 3.14: Histogram of number of storms in terms of the main phase averaged value of *left: α* and *right: α$_{ionospheric}$* in Summer.
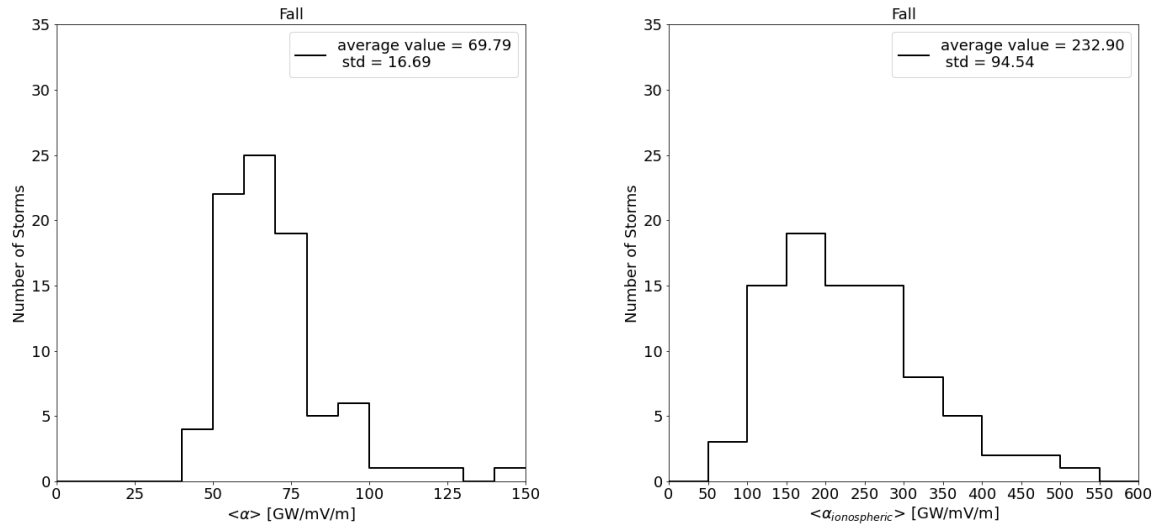
FIGURE 3.15: Histogram of number of storms in terms of the main phase averaged value of *left: α* and *right: α$_{ionospheric}$* in Fall.
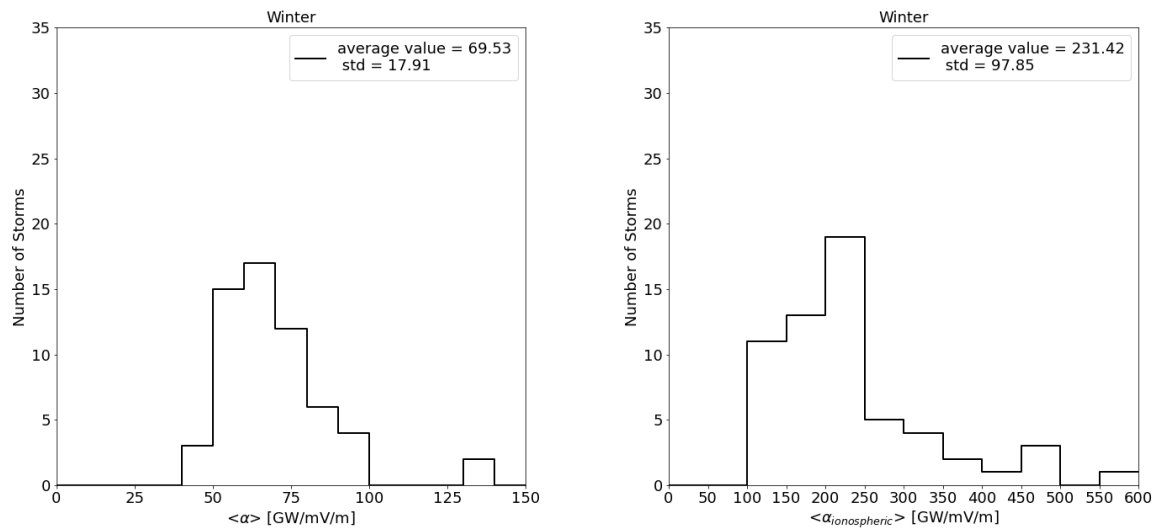
FIGURE 3.16: Histogram of number of storms in terms of the main phase averaged value of *left: α* and *right: α$_{ionospheric}$* in Winter.

Similar to the past, for each category of storms (based on the average value of the Mach number), we calculate the average value of α and $\alpha_{ionospheric}$. As seen in figures 3.17 and 3.18, for the lower Mach number, the ratio of energy dissipated in the ring current and ionosphere to the VB_s is smaller. In other words, As the Mach number decreases, the geoeffective length gets smaller.
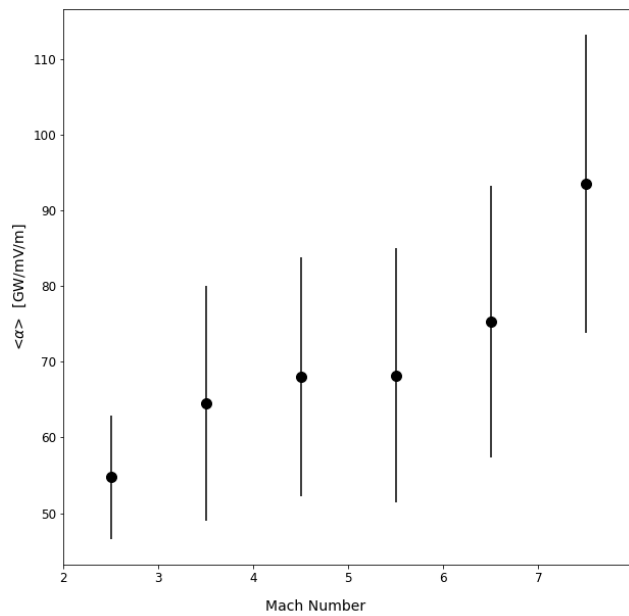
FIGURE 3.17: The average of $< \alpha >$ for different ranges of averaged Mach number.
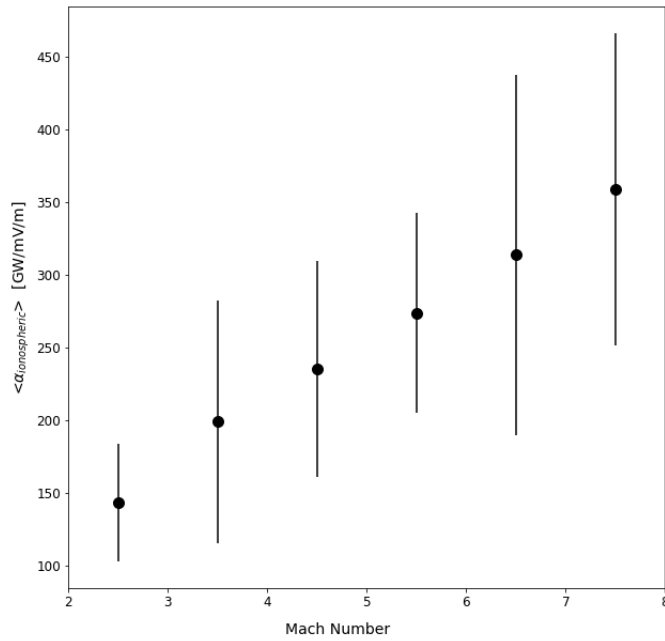
FIGURE 3.18: The average of $< \alpha_{ionospheric} >$ for different ranges of averaged Mach number.

Chapter 4

Comparison of Empirical Models of Ionospheric Heating to Global Simulations

Dayside merging and nightside reconnection produce plasma flow in the ionosphere which can be intense and steady during a geomagnetic storm. The *flow* means that there is an electric field in Earth's reference frame, and this electric field drives auroral electrojet currents that close the Birkeland currents driven by reconnection. The energy dissipated through the Joule heating process is the second most important energy sink after the ring current (Akasofu, 1981) or even sometimes the most important (Harel et al., 1981). Thermospheric responses to Joule heating during magnetic storms can be dramatic (Deng et al., 2018). The ionospheric Joule dissipation heats the ionosphere and thermosphere, and so they can expand upward. These upward expansions can cause the enhancement of the ion outflow and satellite drag. Studies often use empirical models

of electric fields and conductivities to estimate Joule heating. These models typically do not represent the variability of electric fields, currents, and conductivities about the average. The contribution of electric-field variance to total Joule heating and its thermosphere/ionosphere effects can be substantial (Richmond, 2021). Therefore, an accurate estimation of the Joule heating rate is necessary to better understand the energy transfer during geomagnetic storms and the coupling mechanism between the solar wind and the thermosphere-ionosphere-magnetosphere system.

Dissipation of energy through Joule heating is due to the current parallel to the electric field ($U_J = \vec{J}.\vec{E}$). Hence the height-integrated Joule heating can be expressed as a function of Pederson conductivity in the reference frame of the neutrals,

$$U_J = \int \sigma_P(h)(E + U \times B)^2 dh \qquad (4.1)$$

where σ_P is the Pederson conductivity, U is the neutral winds, and B is the magnetic field. Calculation of Joule heating rate needs the measurements of Pederson conductivity and electric field over the entire polar region. However, there is still a challenge to monitor these quantities continuously over the entire high latitude region. Ionospheric electric fields and conductivities can be directly measured just *locally* by using rocket-borne instrumentation or with the incoherent scatter radar. Therefore, several empirical models have been developed using geomagnetic indices such as Kp, AE, or AL to estimate the first approximation measure of the global Joule heating rates (Ahn et al., 1983; Baumjohann & Kamide, 1984; Foster et al., 1983). For example, Baumjohann and Kamide

(1984) assumed that the height-integrated ionospheric conductivity simulates substorm activity in the AE index (Spiro et al., 1982; Zhou et al., 2011). However, these empirical models usually use small data sets or have non-realistic assumptions. For instance, Baumjohann and Kamide (1984) assumed he ionospheric electric field is derivable from an electrostatic potential (Kamide et al., 1981).

To estimate the energy dissipated through the Joule heating process, one can use global Magneto-Hydro-Dynamic (MHD) simulations. Palmroth et al. (2004) use the global MHD simulation code GUMICS-4 and find the temporal variation of the Joule heating power during the substorm event is well correlated with a commonly used AE-based empirical model, whereas, during the storm period, the simulated Joule heating is different from the empirical model. Following this work, in this paper, we use the Space Weather Modeling Framework (SWMF) MHD simulation for 19 storm events already done via Community Coordinated Modeling Center (CCMC) to compare the Joule heating power resulting from simulations with empirical models.

4.1 Correlations between SWMF Simulations and Observations, using the SME Index

In this section, we compare an emprical model of Joule heating with the output of the SMWF simulations for 12 magnetic storms with $Dst^* \leq -50$ nT for

the period between 2010 and 2020, listed in table 4.1. As discussed in Chapter 2, the SWMF simulation can run with or without a ring current model. The simulations that we used here all include a ring current module coupled to the magnetosphere MHD model and the ionosphere (except simulation for event 9 Sep. 2015), but the ring current couples only to the northern polar cap. We calculate the Joule heating rate using the emprical formula (Baumjohann and Kamide, 1984; Østgaard, Germany, et al., 2002; Østgaard, Vondrak, et al., 2002) as,

$$U_{JH}(GW) = 0.32AE \ . \tag{4.2}$$

The AE index (Nose et al., 2015) is produced at a 1-min cadence using data from up to 12 magnetometer stations at latitudes that correspond to the average location of the auroral oval. SuperMAG now produces SME, an equivalent to AE, at a 1-min cadence (Gjerloev, 2012). SME is the difference between upper (SMU) and lower (SML) indices. SMU and SML are based on the H-component measured at stations in the latitudes of the auroral oval, with baseline removal carried out. The difference between AE and SME is the number of stations used in their derivation. While AE uses 12 stations, the number of stations used to derive SME increases with time. By using the 1-min data from SuperMag for the SME index in the 4.2 instead of AE, we estimate the energy dissipated through Joule heating for each storm. Furthermore, we use data from AMPERE as a measure of the strength of Filed-aligned current (FAC) during each storm. AMPERE data are obtained by the use of magnetometers over 70 satellites with a cadence of 2 minutes. The magnetic field data provides a global map of FAC (Anderson et al., 2000).

TABLE 4.1: List of Storm Event Simulations used to compare the
simulated JH and the emprical model.

Date	Time of Main Phase	Run Number	Grid
2 May 2010	10-19 UT	Pelin_Erdemir_021419_1	1 M
28 May 2011	06-12 UT	Haonan_Wu_071818_1	18.5 M
5-6 August 2011	19-04 UT	Sean_Blake_042619_4	1 M
26 Septemebr 2011	15-22 UT	Pauline_Dredger_082321_1	1 M
22 January 2012	07-22 UT	Diptiranjan_Rout_060919_1	1 M
24 January 2012	15-20 UT	Joaquin_Diaz_011221_1	1 M
17 June 2012	00-14 UT	Yihua_zheng_113015_1	1 M
15 July 2012	00-19 UT	Pelin_Erdemir_071821_1	1 M
8-9 August 2012	19-08 UT	Sean_Blake_042619_7	1 M
1 November 2012	03-21 UT	Siyuan_Wu_090319_2	2 M
13-14 November 2012	23-08 UT	Siyuan_Wu_120519_2	1 M
9 September 2015	00-13 UT	Lei_Cai_071720_1	2 M

In the next step, we went through the CCMC database and collected the
SWMF simulations that have already been done for these storms. We compare
the solar wind inputs of the simulations to the 1-minute OMNI data provided by
CDAWeb for each event. We only accept the simulations that their inputs are in
perfect agreement with OMNI data. 4.1 illustrates two examples of the accepted
storm event comparing solar wind data from OMNI with the simulation input.

(A) 6 August 2011   (B) 14 November 2012
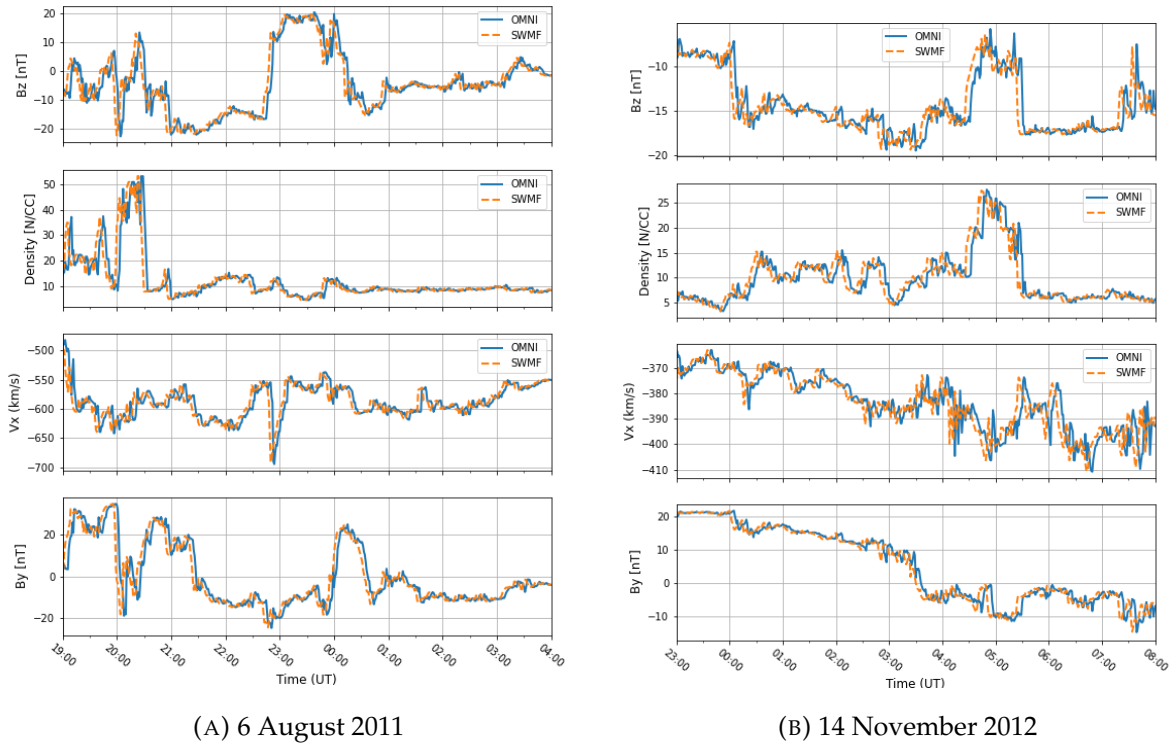
FIGURE 4.1: *Left:* The solar wind data from OMNI and SWMF input for the magnetic storm happened on 6 August 2011. The simulation input and OMNI data are highly correlated with C.C. of 0.99 with 4 minutes timelag. *Right:* The solar wind data from OMNI and SWMF input for the magnetic storm happened on 14 November 2012. The simulation input and OMNI data are highly correlated with C.C. of 0.99 with 6 minutes timelag.

We find that good agreement of the simulation input with the OMNI data does not necessarily result in a good correlation of empirical and SWMF Joule heatings. For instance, although in both cases shown in 4.1 , the inputs of SWMF simulations of the storms are consistent with the OMNI data, the resulting Joule heating is highly correlated with the empirical model in the first event (6 August 2011), whereas it is not in the second event (14 November 2012) as illustrated in figure 4.2.
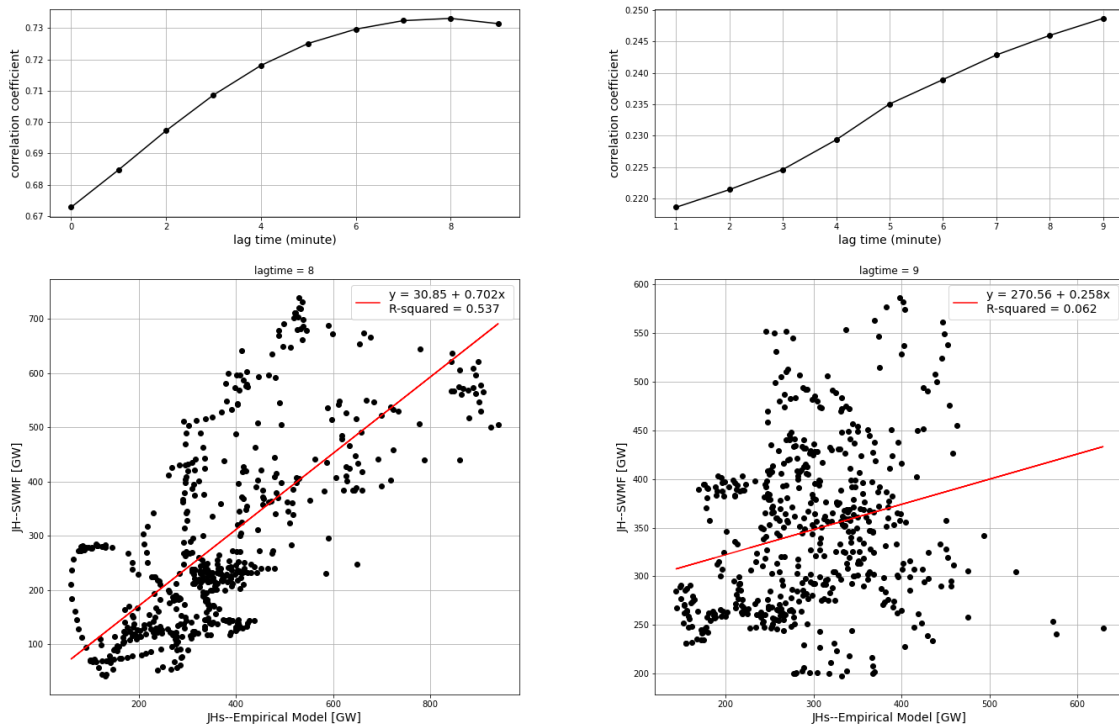
(A) 6 August 2011   (B) 14 November 2012

FIGURE 4.2: *Left: top-panel-*The correlation coefficient of Joule heating resulting from the empirical model and SWMF simulations as a function of lagtime between data. *left: bottom-panel-*The linear relationship of Joule heating using the empirical model and SWMF simulations for the storm happened on 6 August 2011. *Right: top-panel-* The correlation coefficient of Joule heating resulted from the empirical model and SWMF simulations as a function of lagtime between data; *Right: bottom-panel-*The linear relationship of Joule heating using the empirical model and SWMF simulations for the storm that happened on 14 November 2012.

Considering the lagtime between ionospheric data and the output of the

SMWF simulations, generally, in all 12 events corresponding to 142 hours of observation and simulation, SWMF simulations predict a smaller amount of dissipated heating energy than the empirical model for approximately half of the data points.
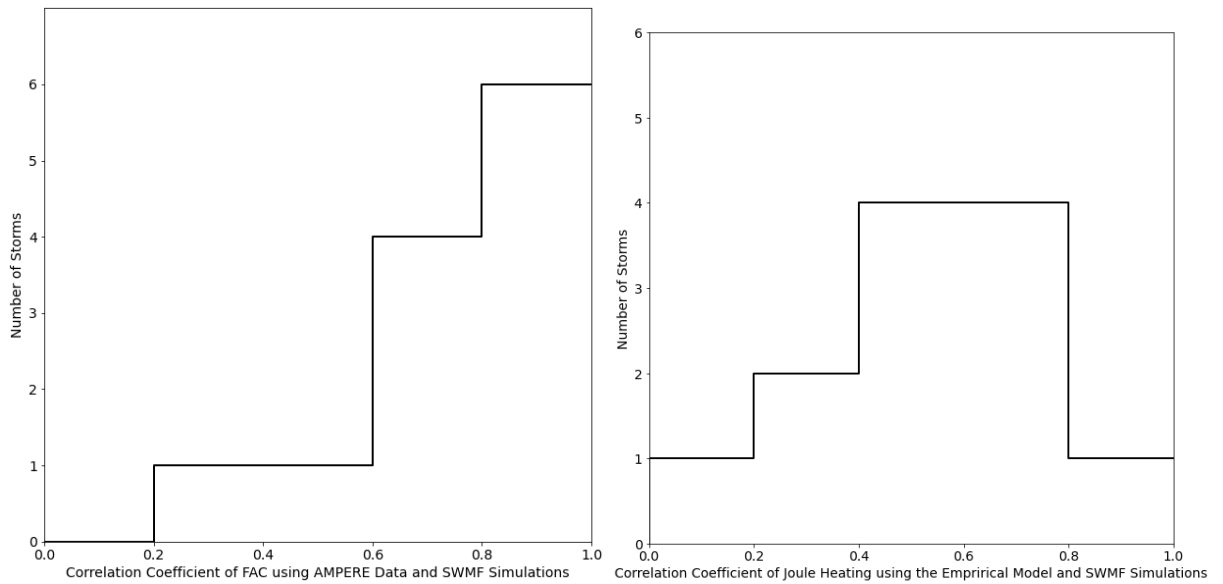
FIGURE 4.3: *Left:*The correlation coeffient of Field-aligned currents using AMPERE data model and SWMF simulations. *Right:*The correlation coeffient of Joule heating resulted from the emprical model and SWMF simulations.
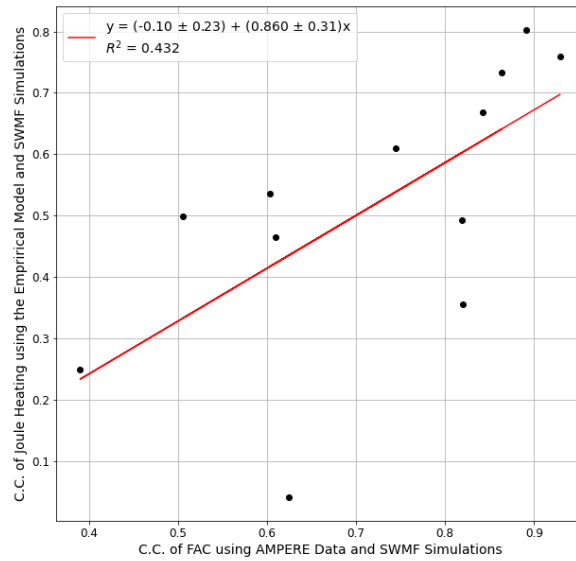
FIGURE 4.4: Correlation coefficient of Joule heating as a function of correlation coefficient of Field-aligned currents for storms in our sample.

We calculate the correlation coefficient between Joule heating using the empirical model and SWMF simulations for all storms. Additionally, we investigate the correlation between AMPERE data of FAC and the ionospheric current resulting from the simulations. Figure 4.3 shows the histogram of the number of events as a function of their correlation coefficient for both cases of Joule heating and Filed-aligned current.

As represented in figure 4.4 we find that the correlation coefficient between Joule heatings increases by increasing the correlation coefficient between currents.

4.2 Correlations between AE and Joule Heating using SWMF Simulations

To investigate the relationship between Joule heating and the AE index, we use the simulations of 13 magnetic storms with $Dst^* \leq -50$ nT. The information of these events are summarized in table 4.2. For each storm, we find the best linear fit between Joule heating and the AE index, both outputted from the simulations, shown in figures 4.5-4.11. Taking the average of all storms' best fits for the Joule heating dissipated energy as a function of the AE index, we can write

$$U_{JH}(GW) = 0.71AE + 32 \ . \tag{4.3}$$

Comparing this result to (4.2), one can conclude that the SWMF model predicts a greater dependency on the AE index for the Joule heating than empirical models such as (4.2). One possible reason for the inconsistency is that the SWMF model does not predict the AE index well (Haiducek et al., 2017; Kitamura et al., 2008) .

TABLE 4.2: List of Storm Event Simulations used to study the relationship between simulated JH and the AE index.

Date	Time of Main Phase	Run Number	Grid
17 September 2000	19-24 UT	Sean_Blake_042619_1	1 M
20 April 2002	03-07 UT	Sean_Blake_040519_6	1 M
23 May 2002	11-18 UT	Luning_Xu_060519_5	1 M
7-8 September 2002	16-01 UT	Sean_Blake_040519_3	1 M
29 May 2003	11-24 UT	Luning_Xu_061419_6	1 M
18 August 2003	01-16 UT	Sean_Blake_042619_2	1 M
5-6 August 2011	19-04 UT	Sean_Blake_042619_4	1 M
26 Septemebr 2011	15-22 UT	Pauline_Dredger_082321_1	1 M
22 January 2012	07-22 UT	Diptiranjan_Rout_060919_1	1 M
24 January 2012	15-20 UT	Joaquin_Diaz_011221_1	1 M
1 November 2012	03-21 UT	Siyuan_Wu_090319_2	1 M
13-14 November 2012	23-08 UT	Siyuan_Wu_120519_2	1 M
17 March 2013	06-11 UT	Pelin_Erdemir_071821_3	1 M
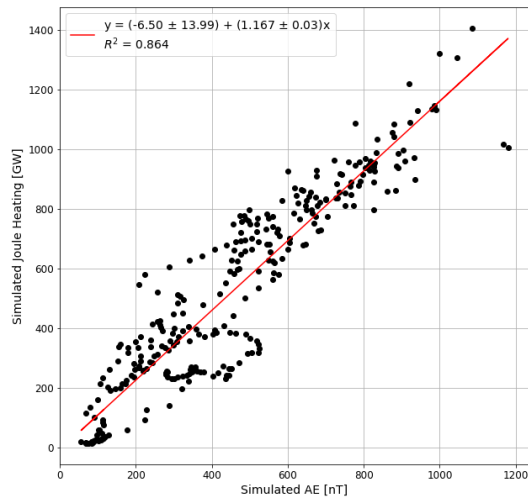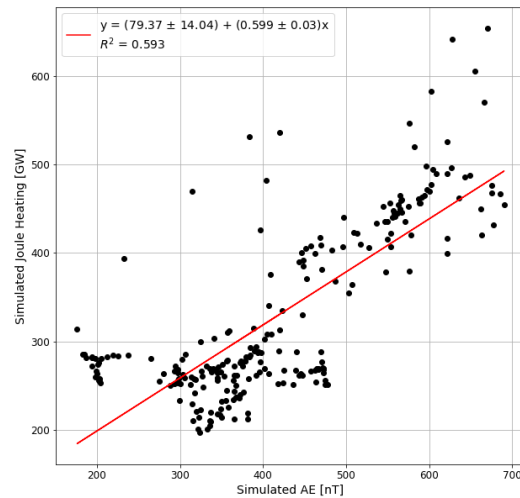
(A) 17 September 2000   (B) 20 April 2002

FIGURE 4.5: Simulated Joule heating vs. simulated AE index for the events: *left*-17 September 2000; *right*- 20 April 2002.
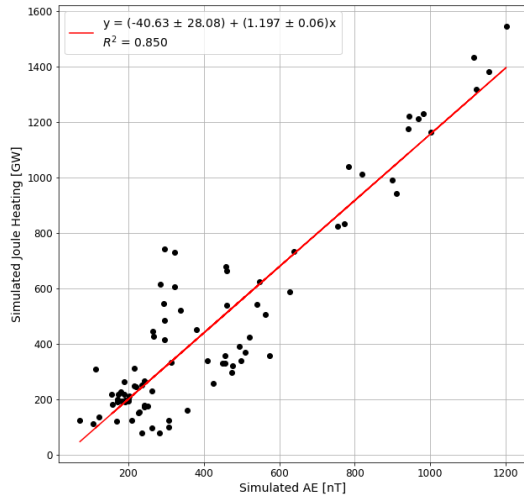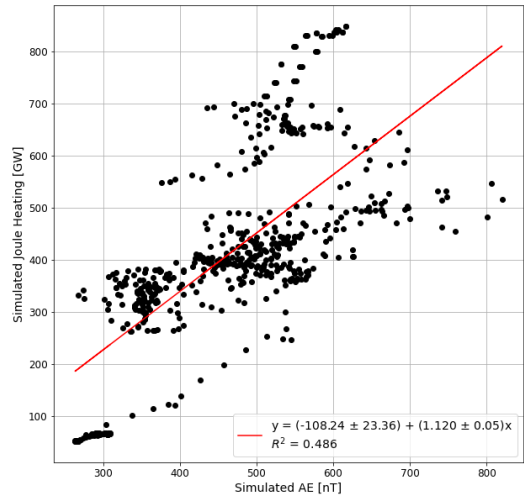
(A) 23 May 2002   (B) 7-8 September 2002

FIGURE 4.6: Simulated Joule heating vs. simulated AE index for
the events: *left*-23 May 2002; *right*- 7-8 September 2002.
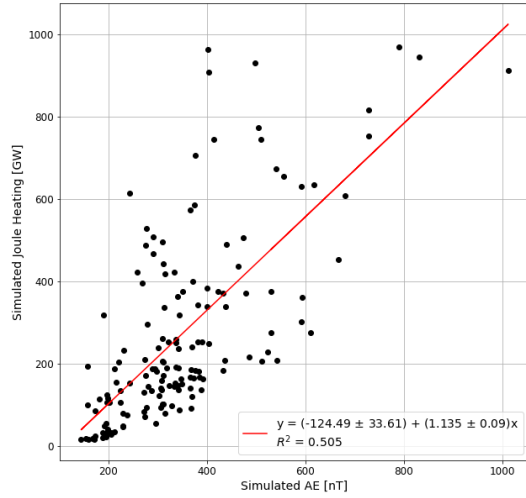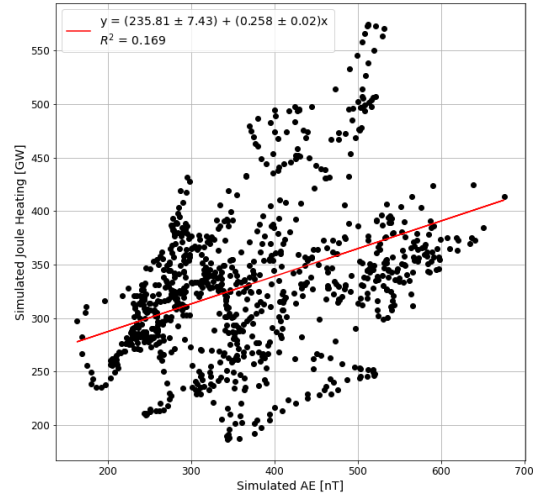
(A) 29 May 2003   (B) 18 August 2003

FIGURE 4.7: Simulated Joule heating vs. simulated AE index for
the events: *left*-29 May 2003; *right*- 18 August 2003.
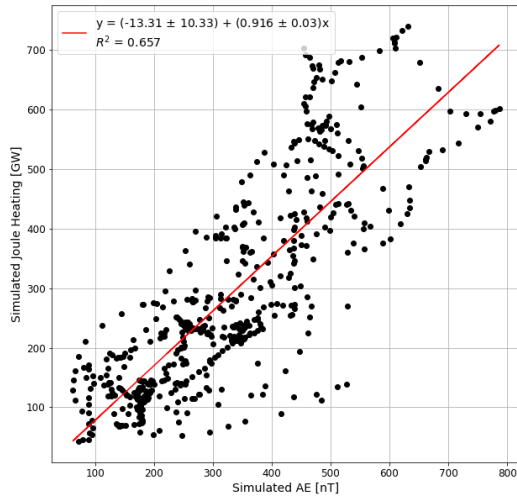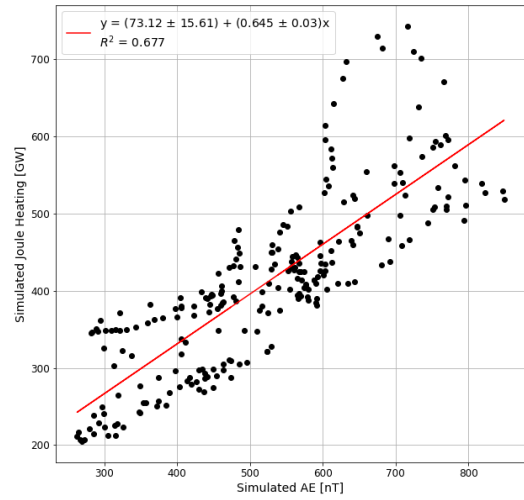
(A) 5-6 August 2011   (B) 26 September 2011

FIGURE 4.8: Simulated Joule heating vs. simulated AE index for
the events: *left-*5-6 August 2011; *right-* 26 Septemebr 2011.
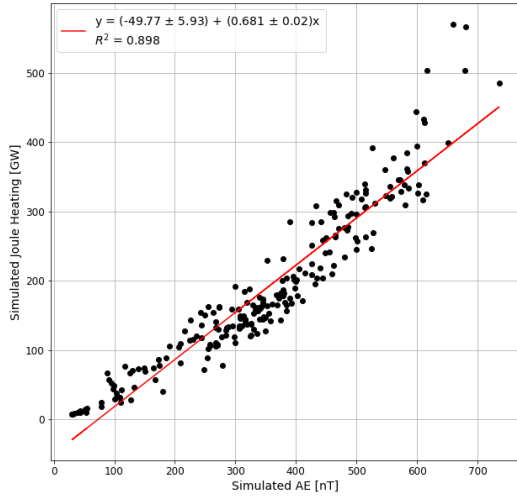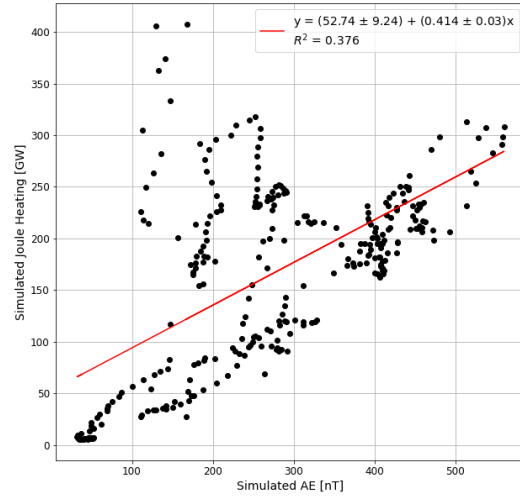
(A) 22 January 2012 (B) 24 January 2012

FIGURE 4.9: Simulated Joule heating vs. simulated AE index for
the events: *left*-22 January 2012; *right*- 24 January 2012.
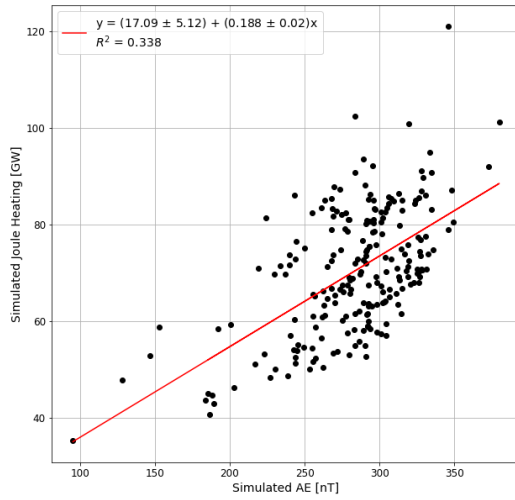
(A) 1 November 2012
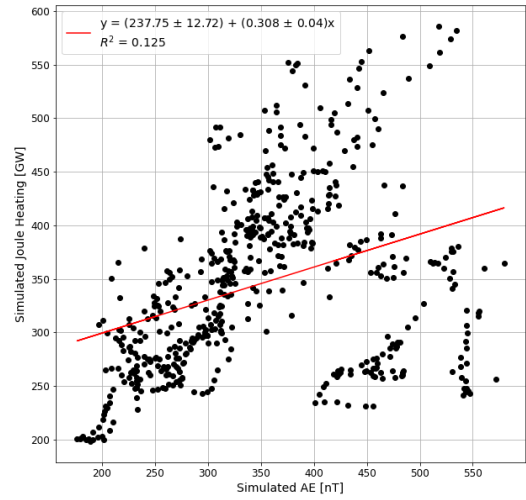
(B) 13-14 November 2012

FIGURE 4.10: Simulated Joule heating vs. simulated AE index for
the events: *left*-1 November 2012; *right*- 13-14 November 2012.
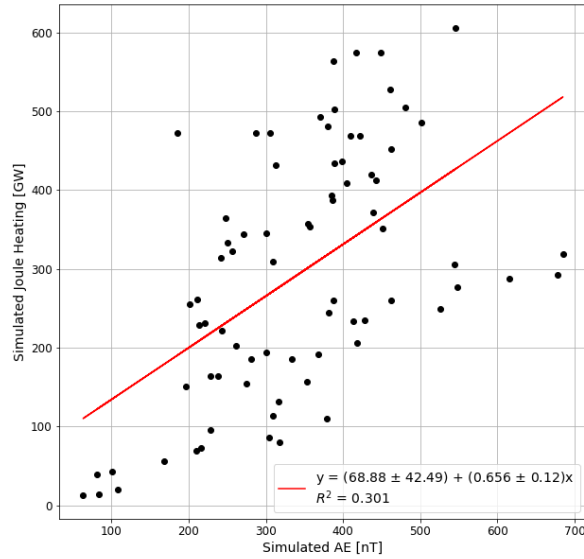
[17 March 2013]

FIGURE 4.11: Simulated Joule heating vs. simulated AE index for the event 17 March 2013.

Chapter 5

Conclusion and Future Studies

Joseph Borvosky in (Borovsky, 2021, Table 1) collected Nine outstanding questions in our physical and quantitative understanding of how the solar wind couples to the magnetosphere-ionosphere system. During my Ph.D. I have studied two of these nine questions:

- *How does the viscous interaction work, and what are the controlling factors?*

- *How does polar-cap potential saturation work?*

In this study, we investigate the role of the solar wind parameters, particularly the magnetosonic Mach number and solar wind density, in controlling and describing the energy transfer into the magnetosphere-ionosphere system under two different conditions: 1) when the ionospheric potential is saturated and 2) during the viscous-dominated event.

Furthermore, we analyze about 320 magnetic storms with $Dst^* \leq -50nT$. We study the different kinds of energy dissipation during the main phase of

these storms using both observations and global magnetohydrodynamics simulations.

Moreover, we compare the empirical model of ionospheric heating with the MHD simulations to better understand energy transfer during the main phase of magnetic storms.

The output of this dissertation can be classified into five categories:

- As discussed in the Introduction 1, the role of the force balance in the magnetosheath is essential to the understanding of the physics of energy transfer to the magnetosphere-ionosphere system during geomagnetic storms. Lower values of solar wind magnetosonic Mach number are responsible for reducing the geoeffective length and the saturation of the polar cap potential. We show in Chapter 2 that the solar wind density variations are responsible for driving the SME index, not only during the January 10, 1997 event (Shue & Kamide, 2001), but also during the main phase of many storms. In fact, the strong correlation between the solar wind density and the SME index results from the saturation of the ionosphere potential. In this regime, the solar wind density becomes a controlling factor for the integrated dayside merging rate and ionospheric potential.

- The current paradigm for classifying geomagnetic storms is based on the Dst index. However, this paradigm is missing the critical physical process: the ring current injection rate does not saturate while the transpolar potential saturates (Lopez et al., 2009; Russell et al., 2001). In Chapter 3

We show that for lower Mach numbers, the correlation between the ionospheric power and the Dst index decreases. Therefore, the Dst index is a weak predictor of the ionospheric power for storms with low Mach numbers, which tend to be the large storms when the prediction of ionospheric power dissipation would be particularly important for space weather.

- Furthermore, in Chapter 3, we also show that the ionospheric indices and the geoeffectiveness of the solar wind are less correlated for the lower Mach number. This result is consistent with the force-balance model because in the saturation regime, by increasing the solar wind energy input, the ionospheric potential remains the same, and the energy dissipates in the ring current and causes the enhancement of the ring current injection rate.

- During geomagnetic storms, the energy dissipated through the Joule heating process is the second most crucial energy sink after the ring current (Akasofu, 1981) or even sometimes the most important (Harel et al., 1981). Therefore, in Chapter 4, we compare the empirical models of the Joule heating power with the Space Weather Modeling Framework (SWMF) MHD simulation for 12 storm events already done via Community Coordinated Modeling Center (CCMC) to better understand the energy transfer during geomagnetic storms and the coupling mechanism between the solar wind and the thermosphere-ionosphere-magnetosphere system. We find that the SWMF model predicts a smaller amount of the Joule heating power.

Moreover, we find that events with a high correlation between the simulated ionospheric current and the AMPERE currents show a higher correlation between the simulated Joule heating power and the empirical model.

- Using the SWMF simulations for 13 magnetic storms, we investigate the relationship between the simulated Joule heating and the simulated AE index. We find that the scale factor has to be about two times greater than the empirical models.

5.1   Future Studies

The coupling between the solar wind and the magnetosphere-Ionosphere system is often assumed to be symmetric in the Northern Hemisphere and Southern Hemisphere in the first order. But, the solar-driven conductance in the ionosphere changes significantly through the seasons of a year. This implies that the magnetospherically driven field-aligned currents must be reduced considerably in the winter hemisphere and enhanced in the summer hemisphere (Ridley, 2007). But in our study, we do not see any seasonal differences in the geoeffectiveness. Thus, one possible future study is investigating the seasonal effects in more detail.

In addition to the seasonal effects that can cause asymmetries between the Northern hemisphere and Southern hemispheres, the B_y component of the IMF can cause asymmetry since it has the opposite effects in the Northern and Southern hemispheres (Pettigrew et al., 2010). Therefore, the next step in the study of

coupling solar wind and the magnetosphere-ionosphere system would be to investigate the role of IMF-B_y along with seasonal effects in energy transfer to the ionosphere during the geomagnetic storms. For instance, here are a few questions regarding the IMF-B_y:

- Does the IMF-B_y affect the energy dissipation?

- Using MHD simulations, how would the change of the sign of B_y affect the ionospheric power?

On the other hand, ring current is not generally included in the MHD simulations. In this study, in Chapter 4, we use the SWMF model, which can run with or without a ring current model. Because our main focus of the research was to study ionospheric heating, having ring current as an output of the simulations does not essential. However, since the ring current closes the Birkeland currents, one could ask if there is any significant difference in the dynamic of the ionosphere current using SWMF simulation with and without the ring current model. As such, one of the future studies could be investigating the role of ring current in dynamic and the amount of ionospheric currents using MHD simulations.

Appendix A

List of Storms.

List of Storm Events Used in This Study.

Start times and durations are for the main phase of the storms.

#	Start Date	Start Time (UT)	Duration (hour)	min Dst^*
1	January 11, 2000	14	8	-102
2	January 22, 2000	16	12	-129
3	January 27, 2000	19	7	-66
4	February 5, 2000	17	6	-64
5	February 12, 2000	8	4	-169
6	March 1, 2000	3	13	-65
7	March 31, 2000	5	7	-82
8	April 1, 2000	15	10	-70
9	April 4, 2000	12	7	-74
10	April 6, 2000	16	9	-336
11	April 16, 2000	7	5	-103
12	April 24, 2000	10	5	-81
13	April 27, 2000	8	9	-51

14	May 17, 2000	0	6	-119
15	May 24, 2000	1	4	-173
16	May 29, 2000	16	6	-74
17	June 8, 2000	15	5	-115
18	July 20, 2000	1	9	-112
19	July 22, 2000	6	12	-85
20	July 23, 2000	12	11	-84
21	August 5, 2000	20	10	-76
22	August 10, 2000	20	11	-122
23	August 12, 2000	2	8	-259
24	August 28, 2000	21	10	-83
25	September 1, 2000	23	12	-76
26	September 6, 2000	19	14	-50
27	September 12, 2000	9	11	-97
28	September 17, 2000	19	5	-241
29	September 19, 2000	8	8	-104
30	October 3, 2000	1	12	-100
31	October 4, 2000	7	14	-166
32	October 5, 2000	3	5	-213
33	October 5, 2000	11	3	-216
34	October 12, 2000	23	7	-104
35	October 14, 2000	2	13	-127
36	October 28, 2000	20	8	-146
37	November 4, 2000	3	7	-74

38	November 6, 2000	13	9	-191
39	November 10, 2000	6	7	-123
40	November 18, 2000	18	13	-44
41	November 24, 2000	18	5	-54
42	November 26, 2000	17	4	-77
43	November 26, 2000	22	4	-111
44	November 29, 2000	6	8	-146
45	January 3, 2001	1	6	-56
46	January 24, 2001	10	9	-80
47	January 31, 2001	8	4	-65
48	February 6, 2001	6	3	-57
49	February 13, 2001	17	5	-72
50	March 4, 2001	18	9	-98
51	March 20, 2001	3	11	-170
52	March 27, 2001	19	5	-78
53	March 28, 2001	11	4	-110
54	March 31, 2001	3	6	-429
55	April 8, 2001	13	3	-83
56	April 11, 2001	15	9	-303
57	April 13, 2001	10	6	-101
58	April 18, 2001	1	6	-151
59	April 22, 2001	1	15	-126
60	May 6, 2001	20	9	-57
61	May 9, 2001	12	7	-92

62	June 18, 2001	3	6	-89
63	August 17, 2001	12	10	-140
64	September 13, 2001	2	6	-80
65	September 23, 2001	9	11	-97
66	September 25, 2001	20	6	-131
67	September 30, 2001	23	10	-173
68	October 3, 2001	6	9	-187
69	October 21, 2001	16	6	-227
70	October 28, 2001	3	9	-184
71	October 31, 2001	19	16	-125
72	November 24, 2001	6	10	-247
73	December 21, 2001	14	9	-87
74	December 24, 2001	0	11	-80
75	December 29, 2001	23	7	-84
76	January 19, 2002	8	10	-60
77	February 2, 2002	3	7	-111
78	February 5, 2002	17	4	-114
79	March 18, 2002	23	7	-60
80	March 23, 2002	23	11	-125
81	March 30, 2002	11	8	-61
82	April 17, 2002	8	10	-136
83	April 18, 2002	0	8	-144
84	April 20, 2002	3	4	-179
85	April 23, 2002	5	4	-90

86	May 11, 2002	10	10	-134
87	May 18, 2002	20	11	-81
88	May 23, 2002	11	7	-141
89	May 27, 2002	3	7	-86
90	July 5, 2002	22	8	-67
91	July 12, 2002	7	4	-65
92	August 1, 2002	10	4	-78
93	August 1, 2002	23	7	-125
94	August 4, 2002	1	5	-82
95	August 18, 2002	21	5	-78
96	August 19, 2002	19	6	-89
97	August 20, 2002	18	13	-127
98	September 4, 2002	2	4	-133
99	September 7, 2002	16	9	-208
100	September 11, 2002	12	11	-111
101	October 1, 2002	7	10	-205
102	October 4, 2002	3	6	-165
103	October 24, 2002	13	8	-124
104	November 20, 2002	16	5	-117
105	November 21, 2002	2	9	-156
106	December 19, 2002	7	12	-99
107	December 20, 2002	21	7	-105
108	December 22, 2002	20	16	-90
109	December 26, 2002	21	10	-99

110	January 3, 2003	14	7	-61
111	January 29, 2003	18	7	-88
112	February 4, 2003	1	9	-98
113	February 27, 2003	13	9	-87
114	March 3, 2003	15	10	-92
115	March 16, 2003	16	6	-84
116	March 31, 2003	6	10	-99
117	April 29, 2003	12	15	-90
118	April 30, 2003	21	4	-104
119	May 10, 2003	0	8	-111
120	May 21, 2003	16	11	-98
121	May 29, 2003	18	6	-213
122	June 2, 2003	2	7	-119
123	June 18, 2003	5	5	-171
124	July 12, 2003	2	4	-132
125	July 16, 2003	3	11	-121
126	July 26, 2003	16	5	-80
127	August 5, 2003	22	5	-86
128	August 18, 2003	1	15	-166
129	September 9, 2003	18	7	-65
130	September 23, 2003	22	10	-84
131	October 14, 2003	20	3	-113
132	November 4, 2003	6	5	-105
133	November 20, 2003	12	9	-456

134	November 22, 2003	13	10	-110
135	January 15, 2004	12	5	-70
136	January 22, 2004	10	4	-158
137	January 23, 2004	12	6	-101
138	February 11, 2004	10	8	-123
139	March 9, 2004	11	13	-99
140	April 3, 2004	14	11	-141
141	April 5, 2004	16	4	-91
142	April 23, 2004	11	5	-61
143	July 16, 2004	22	5	-100
144	July 22, 2004	20	7	-114
145	July 25, 2004	9	8	-170
146	July 26, 2004	22	5	-142
147	July 27, 2004	4	10	-196
148	August 30, 2004	10	13	-158
149	October 12, 2004	21	11	-72
150	November 7, 2004	19	12	-404
151	November 9, 2004	11	5	-172
152	November 9, 2004	18	4	-249
153	November 10, 2004	4	6	-293
154	January 7, 2005	21	4	-126
155	January 12, 2005	2	6	-81
156	January 17, 2005	15	3	-111
157	January 17, 2005	23	3	-105

158	January 21, 2005	17	6	-142
159	February 17, 2005	23	4	-106
160	April 4, 2005	14	13	-94
161	April 11, 2005	16	14	-86
162	April 29, 2005	17	5	-56
163	May 8, 2005	11	8	-139
164	May 15, 2005	5	4	-284
165	May 20, 2005	4	4	-110
166	May 30, 2005	6	8	-138
167	June 4, 2005	13	8	-57
168	June 12, 2005	17	8	-125
169	July 9, 2005	4	15	-78
170	July 10, 2005	11	10	-124
171	July 17, 2005	21	10	-90
172	July 27, 2005	22	8	-68
173	August 24, 2005	9	3	-242
174	August 31, 2005	12	8	-148
175	September 15, 2005	9	8	-103
176	October 31, 2005	7	14	-96
177	December 9, 2005	19	12	-52
178	January 25, 2006	18	10	-73
179	March 6, 2006	16	11	-76
180	April 5, 2006	1	15	-106
181	April 9, 2006	0	8	-103

182	April 14, 2006	0	10	-121
183	April 22, 2006	0	4	-68
184	May 6, 2006	19	3	-82
185	July 28, 2006	1	4	-78
186	August 7, 2006	1	7	-80
187	August 19, 2006	10	15	-107
188	September 23, 2006	17	12	-77
189	November 9, 2006	17	10	-93
190	November 30, 2006	3	11	-95
191	December 14, 2006	21	8	-185
192	January 29, 2007	12	6	-77
193	March 24, 2007	0	9	-90
194	April 1, 2007	0	9	-90
195	May 23, 2007	7	7	-80
196	July 10, 2007	22	5	-58
197	July 20, 2007	7	5	-54
198	October 25, 2007	12	10	-74
199	November 20, 2007	9	12	-82
200	March 9, 2008	1	5	-114
201	March 26, 2008	10	10	-73
202	June 14, 2008	17	7	-60
203	July 12, 2008	1	8	-58
204	September 3, 2008	21	8	-73
205	October 11, 2008	7	5	-79

206	July 22, 2009	1	5	-111
207	August 6, 2009	2	6	-60
208	May 2, 2010	10	9	-99
209	May 29, 2010	0	14	-98
210	August 3, 2010	19	7	-103
211	October 11, 2010	9	10	-100
212	January 6, 2011	20	5	-68
213	February 4, 2011	17	5	-92
214	February 14, 2011	18	5	-65
215	March 1, 2011	9	6	-115
216	March 10, 2011	18	12	-103
217	April 6, 2011	9	10	-82
218	April 12, 2011	4	6	-70
219	May 28, 2011	6	6	-104
220	August 5, 2011	19	9	-143
221	September 9, 2011	13	5	-97
222	September 17, 2011	7	9	-96
223	September 26, 2011	15	7	-141
224	October 24, 2011	21	5	-175
225	January 22, 2012	7	15	-94
226	January 24, 2012	15	5	-74
227	January 25, 2012	8	3	-100
228	February 18, 2012	20	9	-85
229	February 27, 2012	12	8	-77

230	March 7, 2012	4	6	-119
231	March 9, 2012	1	8	-170
232	March 15, 2012	14	7	-114
233	April 23, 2012	17	12	-141
234	June 17, 2012	0	14	-116
235	July 15, 2012	0	19	-161
236	July 28, 2012	13	10	-53
237	September 30, 2012	23	6	-142
238	October 8, 2012	19	7	-123
239	October 13, 2012	1	7	-112
240	November 1, 2012	3	18	-86
241	November 13, 2012	23	9	-129
242	November 23, 2012	22	8	-64
243	January 17, 2013	13	5	-65
244	March 1, 2013	8	3	-87
245	March 17, 2013	6	5	-119
246	June 1, 2013	1	8	-152
247	June 28, 2013	12	19	-128
248	July 6, 2013	0	19	-107
249	July 9, 2013	21	15	-74
250	July 14, 2013	12	11	-102
251	October 8, 2013	20	6	-94
252	November 9, 2013	1	8	-104
253	December 8, 2013	0	9	-88

254	February 27, 2014	17	5	-126
255	April 11, 2014	17	17	-110
256	April 29, 2014	20	14	-89
257	August 27, 2014	3	16	-103
258	September 12, 2014	19	5	-117
259	December 23, 2014	19	7	-79
260	January 7, 2015	7	5	-129
261	February 17, 2015	20	5	-88
262	March 2, 2015	1	8	-81
263	April 9, 2015	22	7	-81
264	April 10, 2015	23	11	-98
265	May 13, 2015	0	7	-106
266	June 8, 2015	5	4	-101
267	June 22, 2015	18	3	-175
268	June 23, 2015	0	5	-228
269	July 13, 2015	2	10	-81
270	July 23, 2015	3	6	-85
271	August 15, 2015	9	4	-91
272	August 23, 2015	6	3	-71
273	August 26, 2015	13	9	-92
274	August 27, 2015	14	7	-115
275	August 28, 2015	2	8	-113
276	September 9, 2015	0	13	-123
277	September 20, 2015	6	6	-96

278	October 7, 2015	13	10	-148
279	October 18, 2015	7	3	-74
280	November 6, 2015	19	12	-116
281	December 14, 2015	15	5	-75
282	December 20, 2015	12	11	-177
283	December 31, 2015	11	5	-81
284	December 31, 2015	18	7	-128
285	January 20, 2016	4	13	-119
286	February 2, 2016	20	7	-75
287	March 6, 2016	15	7	-131
288	March 14, 2016	19	13	-73
289	April 2, 2016	14	10	-79
290	April 7, 2016	17	8	-86
291	May 21, 2016	1	8	-45
292	July 20, 2016	0	8	-56
293	September 1, 2016	1	9	-83
294	September 19, 2016	6	5	-57
295	October 13, 2016	6	12	-119
296	November 10, 2016	10	8	-90
297	March 27, 2017	4	11	-101
298	April 4, 2017	4	4	-69
299	April 19, 2017	23	6	-67
300	April 21, 2017	15	7	-64
301	May 27, 2017	21	11	-148

302	August 4, 2017	5	10	-58
303	August 31, 2017	6	6	-79
304	September 7, 2017	21	5	-166
305	September 12, 2017	20	5	-84
306	September 14, 2017	12	9	-76
307	December 4, 2017	16	6	-67
308	March 9, 2018	23	8	-60
309	April 20, 2018	0	10	-96
310	May 5, 2018	11	8	-73
311	August 25, 2018	14	18	-203
312	September 21, 2018	21	7	-70
313	October 7, 2018	10	12	-79
314	November 4, 2018	9	11	-57

Bibliography

Ahn, B.-H., Akasofu, S.-I., & Kamide, Y. (1983). The joule heat production rate and the particle energy injection rate as a function of the geomagnetic indices ae and al. *Journal of Geophysical Research: Space Physics*, *88*(A8), 6275–6287.

Akasofu, S.-I. (1981). Energy coupling between the solar wind and the magnetosphere. *Space Science Reviews*, *28*(2), 121–190.

Anderson, B. J., Takahashi, K., & Toth, B. A. (2000). Sensing global birkeland currents with iridium® engineering magnetometer data. *Geophysical Research Letters*, *27*(24), 4045–4048.

Axford, W. I., & Hines, C. O. (1961). A unifying theory of high-latitude geophysical phenomena and geomagnetic storms. *Canadian Journal of Physics*, *39*(10), 1433–1464.

Axford, W. (1964). Viscous interaction between the solar wind and the earth's magnetosphere. *Planetary and Space Science*, *12*(1), 45–53.

Bargatze, L., McPherron, R., & Baker, D. (1985). *Solar wind-magnetosphere energy input functions* (tech. rep.). California Univ., Los Angeles (USA). Dept. of Earth and Space Sciences . . .

Bartels, J., Heck, N., & Johnston, H. (1939). Main literature on the magnetic three-hour-range index (kennziffer). *Terr. Mag.*, *44*, 411–454.

Baumjohann, W., & Kamide, Y. (1984). Hemispherical joule heating and the ae indices. *Journal of Geophysical Research: Space Physics*, *89*(A1), 383–388.

Bergin, A., Chapman, S. C., & Gjerloev, J. W. (2020). Ae, dst, and their supermag counterparts: The effect of improved spatial resolution in geomagnetic indices. *Journal of Geophysical Research: Space Physics*, *125*(5), e2020JA027828.

Bhattarai, S., & Lopez, R. (2013). Reduction of viscous potential for northward interplanetary magnetic field as seen in the lfm simulation. *Journal of Geophysical Research: Space Physics*, *118*(6), 3314–3322.

Bhattarai, S., Lopez, R., Bruntz, R., Lyon, J., & Wiltberger, M. (2012). Simulation of the polar cap potential during periods with northward interplanetary magnetic field. *Journal of Geophysical Research: Space Physics*, *117*(A4).

Birkeland, K. (1903). Elementary perturbations. *The Norwegian Aurora Polaris Expedition 1902*, *1*, 61–160.

Borovsky, J. E. (2021). Perspective: Is our understanding of solar-wind/magnetosphere coupling satisfactory? *Frontiers in Astronomy and Space Sciences*, *8*, 5.

Bruntz, R., Lopez, R., Wiltberger, M., & Lyon, J. (2012). Investigation of the viscous potential using an mhd simulation. *Journal of Geophysical Research: Space Physics*, *117*(A3).

Burton, R., McPherron, R., & Russell, C. (1975). An empirical relationship between interplanetary conditions and dst. *Journal of geophysical research*, *80*(31), 4204–4214.

Campbell, W. H. (1996). Dst is not a pure ring-current index.

Carovillano, R. L., & Maguire, J. J. (1968). Magnetic energy relationships in the magnetosphere. *Physics of the magnetosphere* (pp. 290–300). Springer.

Chapman, S., & Ferraro, V. (1941). The geomagnetic ring-current: I—its radial stability. *Terrestrial Magnetism and Atmospheric Electricity*, *46*(1), 1–6.

Chapman, S., & Ferraro, V. C. (1931). A new theory of magnetic storms. *Terrestrial Magnetism and Atmospheric Electricity*, *36*(2), 77–97.

Cowley, S. (1982). The causes of convection in the earth's magnetosphere: A review of developments during the ims. *Reviews of Geophysics*, *20*(3), 531–565.

Cowley, S. (1984). Solar wind control of magnetospheric convection. *Achievements of the International Magnetospheric Study (IMS)*, *217*, 483.

Cowley, S., Morelli, J., & Lockwood, M. (1991). Dependence of convective flows and particle precipitation in the high-latitude dayside ionosphere on the x and y components of the interplanetary magnetic field. *Journal of Geophysical Research: Space Physics*, *96*(A4), 5557–5564.

Crooker, N. (1992). Reverse convection. *Journal of Geophysical Research: Space Physics*, *97*(A12), 19363–19372.

Daglis, I. A., Thorne, R. M., Baumjohann, W., & Orsini, S. (1999). The terrestrial ring current: Origin, formation, and decay. *Reviews of Geophysics*, *37*(4), 407–438.

Deng, Y., Sheng, C., Tsurutani, B. T., & Mannucci, A. J. (2018). Possible influence of extreme magnetic storms on the thermosphere in the high latitudes. *Space Weather*, *16*(7), 802–813.

Dessler, A., & Parker, E. N. (1959). Hydromagnetic theory of geomagnetic storms. *Journal of Geophysical Research*, *64*(12), 2239–2252.

Dubyagin, S., Ganushkina, N., Kubyshkina, M., & Liemohn, M. (2014). Contribution from different current systems to sym and asy midlatitude indices. *Journal of Geophysical Research: Space Physics*, *119*(9), 7243–7263.

Dungey, J. W. (1961). Interplanetary magnetic field and the auroral zones. *Physical Review Letters*, *6*(2), 47.

Dungey, J. (1953). Lxxvi. conditions for the occurrence of electrical discharges in astrophysical systems. *The London, Edinburgh, and Dublin Philosophical Magazine and Journal of Science*, *44*(354), 725–738.

Dungey, J. (1965). The length of the magnetospheric tail. *Journal of Geophysical Research*, *70*(7), 1753–1753.

Foster, J., St.-Maurice, J.-P., & Abreu, V. (1983). Joule heating at high latitudes. *Journal of Geophysical Research: Space Physics*, *88*(A6), 4885–4897.

Frank, L. A. (1967). On the extraterrestrial ring current during geomagnetic storms. *Journal of Geophysical Research*, *72*(15), 3753–3767.

Giovanelli, R. (1947). Magnetic and electric phenomena in the sun's atmosphere associated with sunspots. *Monthly Notices of the Royal Astronomical Society*, *107*(4), 338–355.

Giovanelli, R. (1948). Chromospheric flares. *Monthly Notices of the Royal Astronomical Society*, *108*(2), 163–176.

Giovanelli, R. G. (1939). The relations between eruptions and sunspots. *The Astrophysical Journal*, *89*, 555.

Gjerloev, J. (2012). The supermag data processing technique. *Journal of Geophysical Research: Space Physics*, *117*(A9).

Gombosi, T., Toth, G., Volberg, O., Sokolov, I., Ridley, A., de Zeeuw, D., Hansen, K., Chesney, D., Powell, K., Kane, K., et al. (2004). Space weather modeling framework: An overview. *AGU Spring Meeting Abstracts*, *2004*, SM54A–02.

Gonzalez, W., Joselyn, J.-A., Kamide, Y., Kroehl, H. W., Rostoker, G., Tsurutani, B., & Vasyliunas, V. (1994). What is a geomagnetic storm? *Journal of Geophysical Research: Space Physics*, *99*(A4), 5771–5792.

Graham, G. (1724). Iv. an account of observations made of the variation of the horizontal needle at london, in the latter part of the year 1772, and beginning of 1723. *Philosophical Transactions of the Royal Society of London*, *33*(383), 96–107.

Greenspan, M., & Hamilton, D. (2000). A test of the dessler-parker-sckopke relation during magnetic storms. *Journal of Geophysical Research: Space Physics*, *105*(A3), 5419–5430.

Haiducek, J. D., Welling, D. T., Ganushkina, N. Y., Morley, S. K., & Ozturk, D. S. (2017). Swmf global magnetosphere simulations of january 2005: Geomagnetic indices and cross-polar cap potential. *Space Weather*, *15*(12), 1567–1587.

Harel, M., Wolf, R., Reiff, P., Spiro, R., Burke, W., Rich, F., & Smiddy, M. (1981). Quantitative simulation of a magnetospheric substorm 1. model logic and overview. *Journal of Geophysical Research: Space Physics*, *86*(A4), 2217–2241.

Hasegawa, H., Fujimoto, M., Phan, T., Reme, H., Balogh, A., Dunlop, M., Hashimoto, C., & TanDokoro, R. (2004). Rolled-up kelvin-helmholtz vortices and associated solar wind entry at earth's magnetopause. *Nature*, *430*, 755–758.

Heppner, J., Ness, N., Scearce, C., & Skillman, T. (1963). Explorer 10 magnetic field measurements. *Journal of Geophysical Research*, *68*(1), 1–46.

Hesse, M., & Cassak, P. (2020). Magnetic reconnection in the space sciences: Past, present, and future. *Journal of Geophysical Research: Space Physics*, *125*(2), e2018JA025935.

Hoyle, F. (2014). *Some recent researches in solar physics*. Cambridge University Press.

Iijima, T., & Potemra, T. A. (1976). The amplitude distribution of field-aligned currents at northern high latitudes observed by triad. *Journal of Geophysical Research*, *81*(13), 2165–2174.

Iyemori, T., Araki, T., Kamei, T., & Takeda, M. (1992). Mid-latitude geomagnetic indices asy and sym (provisional) no. 1 1989. *Data Analysis Center for Geomagnetism and Space Magnetism, Kyoto University, Kyoto*.

Iyemori, T. (1990). Storm-time magnetospheric currents inferred from mid-latitude geomagnetic field variations. *Journal of geomagnetism and geoelectricity*, *42*(11), 1249–1265.

Kalegaev, V., Ganushkina, N. Y., Pulkkinen, T., Kubyshkina, M., Singer, H., & Russell, C. (2005). Relation between the ring current and the tail current during magnetic storms. *Annales Geophysicae*, *23*(2), 523–533.

Kamide, Y., Richmond, A., & Matsushita, S. (1981). Estimation of ionospheric electric fields, ionospheric currents, and field-aligned currents from ground magnetic records. *Journal of Geophysical Research: Space Physics*, *86*(A2), 801–813.

Kitamura, K., Shimazu, H., Fujita, S., Watari, S., Kunitake, M., Shinagawa, H., & Tanaka, T. (2008). Properties of ae indices derived from real-time global simulation and their implications for solar wind-magnetosphere coupling. *Journal of Geophysical Research: Space Physics*, *113*(A3).

Krieger, A., Timothy, A., & Roelof, E. (1973). A coronal hole and its identification as the source of a high velocity solar wind stream. *Solar Physics*, *29*(2), 505–525.

Lakhina, G. S., & Tsurutani, B. T. (2016). Geomagnetic storms: Historical perspective to modern view. *Geoscience Letters*, *3*(1), 1–11.

Loewe, C., & Prölss, G. (1997). Classification and mean behavior of magnetic storms. *Journal of Geophysical Research: Space Physics*, *102*(A7), 14209–14213.

Lopez, R. E. (2018). The bow shock current system. *Electric Currents in Geospace and Beyond*, *235*, 479.

Lopez, R., Bruntz, R., Mitchell, E., Wiltberger, M., Lyon, J., & Merkin, V. (2010). Role of magnetosheath force balance in regulating the dayside reconnection potential. *Journal of Geophysical Research: Space Physics*, *115*(A12).

Lopez, R., Gonzalez, W., Vasyliūnas, V., Richardson, I., Cid, C., Echer, E., Reeves, G., & Brandt, P. C. (2015). Decrease in sym-h during a storm main phase without evidence of a ring current injection. *Journal of Atmospheric and Solar-Terrestrial Physics*, *134*, 118–129.

Lopez, R., Lyon, J., Mitchell, E., Bruntz, R., Merkin, V., Brogl, S., Toffoletto, F., & Wiltberger, M. (2009). Why doesn't the ring current injection rate saturate? *Journal of Geophysical Research: Space Physics*, *114*(A2).

Lopez, R., Wiltberger, M., Hernandez, S., & Lyon, J. (2004). Solar wind density control of energy transfer to the magnetosphere. *Geophysical research letters*, *31*(8).

Lu, G., Baker, D., McPherron, R., Farrugia, C. J., Lummerzheim, D., Ruohoniemi, J., Rich, F., Evans, D., Lepping, R., Brittnacher, M., et al. (1998). Global energy deposition during the january 1997 magnetic cloud event. *Journal of Geophysical Research: Space Physics*, *103*(A6), 11685–11694.

Mac-Mahon, R. M., & Gonzalez, W. (1997). Energetics during the main phase of geomagnetic superstorms. *Journal of Geophysical Research: Space Physics*, *102*(A7), 14199–14207.

Maggiolo, R., Hamrin, M., De Keyser, J., Pitkänen, T., Cessateur, G., Gunell, H., & Maes, L. (2017). The delayed time response of geomagnetic activity to the solar wind. *Journal of Geophysical Research: Space Physics*, *122*(11), 11–109.

Milan, S. E., Cowley, S., Lester, M., Wright, D., Slavin, J., Fillingim, M., Carlson, C., & Singer, H. (2004). Response of the magnetotail to changes in the open flux content of the magnetosphere. *Journal of Geophysical Research: Space Physics*, *109*(A4).

Murayama, T., Aoki, T., Nakai, H., & Hakamada, K. (1980). Empirical formula to relate the auroral electrojet intensity with interplanetary parameters. *Planetary and Space Science*, *28*(8), 803–813.

Newell, P. T., Sotirelis, T., Liou, K., & Rich, F. (2008). Pairs of solar wind-magnetosphere coupling functions: Combining a merging term with a viscous term works best. *Journal of Geophysical Research: Space Physics*, *113*(A4).

Newell, P., & Gjerloev, J. (2012). Supermag-based partial ring current indices. *Journal of Geophysical Research: Space Physics*, *117*(A5).

Nose, M., Iyemori, T., Sugiura, M., & Kamei, T. (2015). Geomagnetic ae index. *World Data Center for Geomagnetism, Kyoto*, *10*, 15–031.

Nykyri, K., Otto, A., Lavraud, B., Mouikis, C., Kistler, L., Balogh, A., & Reme, H. (2006). Cluster observations of reconnection due to the kelvin-helmholtz instability at the dawnside magnetospheric flank. *Annales Geophysicae*, *24*(10), 2619–2643.

O'Brien, T. P., & McPherron, R. L. (2000). An empirical phase space analysis of ring current dynamics: Solar wind control of injection and decay. *Journal of Geophysical Research: Space Physics*, *105*(A4), 7707–7719.

Østgaard, N., Germany, G., Stadsnes, J., & Vondrak, R. (2002). Energy analysis of substorms based on remote sensing techniques, solar wind measurements, and geomagnetic indices. *Journal of Geophysical Research: Space Physics*, *107*(A9), SMP–9.

Østgaard, N., Vondrak, R., Gjerloev, J., & Germany, G. (2002). A relation between the energy deposition by electron precipitation and geomagnetic indices during substorms. *Journal of Geophysical Research: Space Physics*, *107*(A9), SMP–16.

Palmroth, M., Janhunen, P., Pulkkinen, T., & Koskinen, H. (2004). Ionospheric energy input as a function of solar wind parameters: Global mhd simulation results. *Annales Geophysicae*, *22*(2), 549–566.

Perreault, P., & Akasofu, S. (1978). A study of geomagnetic storms. *Geophysical Journal International*, *54*(3), 547–573.

Pettigrew, E., Shepherd, S., & Ruohoniemi, J. (2010). Climatological patterns of high-latitude convection in the northern and southern hemispheres: Dipole tilt dependencies and interhemispheric comparisons. *Journal of Geophysical Research: Space Physics*, *115*(A7).

Phillips, J., Balogh, A., Bame, S., Goldstein, B., Gosling, J., Hoeksema, J., McComas, D., Neugebauer, M., Sheeley Jr, N., & Wang, Y.-M. (1994). Ulysses at 50° south: Constant immersion in the high-speed solar wind. *Geophysical research letters*, *21*(12), 1105–1108.

Prigancová, A., & Feldstein, Y. I. (1992). Magnetospheric storm dynamics in terms of energy output rate. *Planetary and space science*, *40*(4), 581–588.

Reiff, P. H., Spiro, R. W., & Hill, T. (1981). Dependence of polar cap potential drop on interplanetary parameters. *Journal of Geophysical Research: Space Physics*, *86*(A9), 7639–7648.

Richmond, A. D. (2021). Joule heating in the thermosphere. *Upper Atmosphere Dynamics and Energetics*, 1–18.

Ridley, A. (2007). Effects of seasonal changes in the ionospheric conductances on magnetospheric field-aligned currents. *Geophysical research letters*, *34*(5).

Russell, C., Luhmann, J., & Lu, G. (2001). Nonlinear response of the polar ionosphere to large values of the interplanetary electric field. *Journal of Geophysical Research: Space Physics*, *106*(A9), 18495–18504.

Sandhu, J., Rae, I., & Walach, M.-T. (2021). Challenging the use of ring current indices during geomagnetic storms. *Journal of Geophysical Research: Space Physics*, *126*(2), e2020JA028423.

Sckopke, N. (1966). A general relation between the energy of trapped particles and the disturbance field near the earth. *Journal of Geophysical Research*, *71*(13), 3125–3130.

Seki, K., Nagy, A., Jackman, C., Crary, F., Fontaine, D., Zarka, P., Wurz, P., Milillo, A., Slavin, J., Delcourt, D., et al. (2015). A review of general physical and chemical processes related to plasma sources and losses for solar system magnetospheres. *Space science reviews*, *192*(1), 27–89.

Shue, J.-H., & Kamide, Y. (2001). Effects of solar wind density on auroral electrojets. *Geophysical research letters*, *28*(11), 2181–2184.

Singer, S. F. (1957). A new model of magnetic storms and aurorae. *Eos, Transactions American Geophysical Union*, *38*(2), 175–190.

Singer, S. (1956). Trapped orbits in the earth's dipole field. *Bull. Am. Phys. Soc. Series II*, *1*, 229.

Smith, E. J., & Wolfe, J. H. (1976). Observations of interaction regions and corotating shocks between one and five au: Pioneers 10 and 11. *Geophysical Research Letters*, *3*(3), 137–140.

Smith, P., & Hoffman, R. A. (1973). Ring current particle distributions during the magnetic storms of december 16–18, 1971. *Journal of Geophysical Research*, *78*(22), 4731–4737.

Snyder, C. W., Neugebauer, M., & Rao, U. (1963). The solar wind velocity and its correlation with cosmic-ray variations and with solar and geomagnetic activity. *Journal of Geophysical Research*, *68*(24), 6361–6370.

Spiro, R., Reiff, P. H., & Maher Jr, L. (1982). Precipitating electron energy flux and auroral zone conductances-an empirical model. *Journal of Geophysical Research: Space Physics*, *87*(A10), 8215–8227.

Stepanova, M., Antonova, E., Moya, P., Pinto, V., & Valdivia, J. (2019). Multi-satellite analysis of plasma pressure in the inner magnetosphere during the 1 june 2013 geomagnetic storm. *Journal of Geophysical Research: Space Physics*, *124*(2), 1187–1202.

Sugiura, M., & Chapman, S. (1960). The average morphology of geomagnetic storms with sudden commencement, abhandl. *Akad. Wiss. Goettingen Math. Physik. Kl*, *4*, 53.

Sugiura, M. (1964). Hourly values of equatorial d_< st> for the igy. *Ann. Int. Geophys. Year*, *35*, 9.

Timothy, A., Krieger, A., & Vaiana, G. (1975). The structure and evolution of coronal holes. *Solar Physics*, *42*(1), 135–156.

Turner, N. E., Baker, D., Pulkkinen, T., & McPherron, R. (2000). Evaluation of the tail current contribution to dst. *Journal of Geophysical Research: Space Physics*, *105*(A3), 5431–5439.

Turner, N. E., Mitchell, E. J., Knipp, D. J., & Emery, B. A. (2006). Energetics of magnetic storms driven by corotating interaction regions: A study of geo-effectiveness.

Valdivia, J., Sharma, A., & Papadopoulos, K. (1996). Prediction of magnetic storms by nonlinear models. *Geophysical research letters*, *23*(21), 2899–2902.

Vasyliunas, V. (2005). Relation between magnetic fields and electric currents in plasmas. *Annales Geophysicae*, *23*(7), 2589–2597.

Vasyliūnas, V. M. (2001). Electric field and plasma flow: What drives what? *Geophysical Research Letters*, *28*(11), 2177–2180.

Vasyliūnas, V. M. (2011). The largest imaginable magnetic storm. *Journal of atmospheric and solar-terrestrial physics*, *73*(11-12), 1444–1446.

Vasyliūnas, V. M., & Song, P. (2005). Meaning of ionospheric joule heating. *Journal of Geophysical Research: Space Physics*, *110*(A2).

Walach, M.-T., & Grocott, A. (2019). Superdarn observations during geomagnetic storms, geomagnetically active times, and enhanced solar wind driving. *Journal of Geophysical Research: Space Physics*, *124*(7), 5828–5847.

Weimer, D. (2001). An improved model of ionospheric electric potentials including substorm perturbations and application to the geospace environment modeling november 24, 1996, event. *Journal of Geophysical Research: Space Physics*, *106*(A1), 407–416.

Williams, D. (1981). Ring current composition and sources: An update. *Planetary and Space Science*, *29*(11), 1195–1203.

Zhou, X.-Y., Sun, W., Ridley, A., & Mende, S. (2011). Joule heating associated with auroral electrojets during magnetospheric substorms. *Journal of Geophysical Research: Space Physics*, *116*(A5).